Circular photogalvanic spectroscopy of Rashba splitting in 2D hybrid organic-inorganic perovskite multiple quantum wells

Xiaojie Liu[1], Ashish Chanana[1,2], Uyen Huynh[1], Fei Xue[3,4], Paul Haney[3], Steve Blair[2], Xiaomei Jiang[5*] and Z. V. Vardeny[1*]

[1]: Department of Physics & Astronomy, University of Utah, Salt Lake City, UT 84112, USA

[2]: Department of Electrical Engineering, University of Utah, Salt Lake City, UT 84112, USA

[3]: Center for Nanoscale Science and Technology, National Institute of Standards and Technology, Gaithersburg, MD 20899, USA.

[4]: Institute for Research in Electronics and Applied Physics & Maryland Nanocenter, University of Maryland, College Park, MD 20742, USA

[5]: Department of Physics, University of South Florida, Tampa, FL 33620, USA

*: xjiang@usf.edu

*: val@physics.utah.edu

Abstract

The two-dimensional (2D) Ruddlesden–Popper organic-inorganic halide perovskites such as (2D)-phenylethyl ammonium lead iodide (2D-PEPI) have layered structure that resembles multiple quantum wells (MQW). The heavy atoms in 2D-PEPI contribute a large spin-orbit coupling that influences the electronic band structure. Upon breaking the inversion symmetry, a spin splitting ('Rashba splitting') occurs in the electronic bands. We have studied the spin splitting in 2D-PEPI single crystals using the circular photogalvanic effect (CPGE). We confirm the existence of Rashba splitting at the electronic band extrema of 35±10 meV, and identify the main inversion symmetry breaking direction perpendicular to the MQW planes. The CPGE action spectrum above the bandgap reveals spin-polarized photocurrent generated by ultrafast relaxation of excited photocarriers separated in momentum space. Whereas the helicity dependent photocurrent with below-gap excitation is due to spin-galvanic effect of the ionized spin-polarized excitons, where spin polarization occurs in the spin-split bands due to asymmetric spin-flip.

Main text

Introduction

In recent years the three-dimensional (3D) hybrid organic-inorganic halide perovskites (HOIP) with the general formula of AMX_3, where A is an organic cation such as methylammonium (MA), M a divalent metal cation such as Pb^{2+}, and X^- the halide anion such as I^-, have been extensively studied [1-3]. The superior optical and electronic properties of these semiconductors have opened a wide range of optoelectronic applications such as photovoltaic devices, light emitting diodes and lasers [4-9]. The heavy atoms, namely lead and halogen endow HOIP with large spin orbit coupling (SOC). In the presence of structural inversion symmetry breaking, the SOC leads to spin-splitting of the continuum bands, a phenomenon known as 'Rashba splitting' (see **Fig. 1D**) [10-14]. This may open a new avenue of using HOIP in spin-related optoelectronic and spintronic applications [15-17].

The 2D version of the HOIP are the multilayered Ruddlesden-Popper compounds with the general formula of $A_2A'_{n-1}M_nX_{3n+1}$, with the corner-sharing $[MX_6]^{4-}$ octahedra forming the inorganic perovskite layers separated by the bilayer of interdigitated long chain organic cation A [18,19], where n indicates the number of inorganic perovskite layers. When n>1, a small organic cation A' can also be intercalated in the cube formed by eight corner-sharing $[MX_6]^{4-}$ octahedra. 2D HOIP offer superior stability over the 3D counterparts due to the protection of the hydrophobic organic layer, and tunability owing to the synthesis versatility [18-20]. The 2D HOIP form natural multiple quantum well (MQW) structure in which the inorganic $[MI_6]^{4-}$ layers serve as the potential 'wells' and the organic cation chains are the potential 'wall' (see **Figure 1A**) [21, 22]. The 2D-phenylethyl ammonium lead iodide (2D-PEPI), $(C_6H_5(CH_2)_2NH_3)_2PbI_4$, (n=1) is a model example of such natural MQW. At low temperature (~200K), its crystal structure is monoclinic (space group C2/m)[23, 24]. There is a lack of consensus on the room temperature crystal structure in the literature, with the majority reporting a triclinic structure (space group $P\bar{1}$) [19,25,26]. Both C2/m and $P\bar{1}$ space groups are centrosymmetric; however, responses associated with broken inversion symmetry may still occur due to the presence of interfaces/surfaces in the MQW structure [14,27]. Giant Rashba splitting was inferred in a recent spectroscopic study of 2D-PEPI [28] and has since initiated strong interest in this material [25, 26, 29]. However, a direct observation of a spin-related photocurrent and the symmetry breaking direction are still missing. Furthermore, unlike the well-studied doped III-V semiconductor MQW structures, where free carriers carry the spin photocurrent [30], it is largely unknown what role, if any, the excitons in 2D-PEPI play in the photogeneration of spin current. The circular photogalvanic effect (CPGE) is considered as the most important experiment that verifies the existence of Rashba splitting in the electronic bands [14]. CPGE has been studied in a variety of Rashba type materials including doped GaAs/AlGaAs MQW [31], the polar semiconductor BiTeI [32], 2D transition-metal dichalcogenides [33], and topological insulator [34]. Most recently, the CPGE was studied in bulk methylammonium lead iodide perovskite ($MAPbI_3$) films [35] and single crystal [36]. Here we employ helicity-dependent steady state photocurrent and terahertz (THz) transient emission spectroscopies for studying the CPGE in 2D-PEPI single crystals at room temperature. Our

results confirm the existence of Rashba splitting with energy of 35±10 meV at the bands extrema and identify the main inversion symmetry breaking direction to be perpendicular to the MQW planes. The CPGE action spectrum shows two distinctive features that are respectively associated with the split interband (IB) transition and polarized exciton (EX) excitation.

Results

Continuous wave (CW) photogalvanic (PGE) currents in 2D-PEPI crystal

As an introduction to the optical properties of 2D-PEPI, **Figure 1B** shows the absorption spectrum of a thin film at room temperature (RT). The absorption spectrum has a pronounced peak at E_{ex} ≈2.40 eV due to the exciton absorption, followed by a monotonic increase related to interband absorption, with an onset at ≈2.57 eV [28]. Other than a small blue shift (~5meV), the absorption of film and single crystal is essentially the same, with nearly identical interband absorption edge [25]. At lower temperature the exciton band in 2D-PEPI film splits into two excitons, exciton 1 (EX1) and exciton 2 (EX2) that are ~40 meV apart [28, 37]. The split of the exciton band in 2D-PEPI can be seen even at RT in single crystal that has less disorder than in film, as evident in the reflectivity spectrum shown in **Figure 1B** inset (marked by the two broken lines).

Figure 1C illustrates the experimental geometry used for the helicity dependent photocurrent measurement; the definition of various axis and angles are given in **Figure 1C** caption. We used a quartz $\lambda/4$ plate (QWP) to modulate the light polarization from right circular polarization (RCP, $\sigma+$), to linear polarization (LP), to left circular polarization (LCP, $\sigma-$) by rotating the angle, α between the fast axis of the QWP and the incident light polarization. In addition, the light excitation intensity was modulated at frequency $f=310Hz$ using a mechanical chopper, and the resulting photocurrent vs. α was measured using a phase sensitive technique (see Methods section in the **SI**). Importantly, the CPGE response is obtained at zero bias voltage. We note that the degree of circular polarization, P_{circ} varies with the rotation angle α as $P_{circ}= sin2\alpha$; namely P_{circ} = +1 for RCP (or σ^+) when α=45^0, 225^0..., P_{circ} = -1 for LCP when α=135^0, 315^0..., and P_{circ} = 0 for LP light, when α=90^0, 180^0... [30].

In HOIP the conduction band (CB) bottom consists of J= ½ states, whereas the valence band (VB) top has S=½ states [38]. The optical transition selection rules for in-plane spin polarization require that the component of angular momentum directed along the Rashba effective magnetic field changes by Δm_J=±1. Taking this into consideration, **Figure 1D** shows a schematic in one dimensional **k**-space. When Rashba splitting occurs in the CB and VB, the absorption of RCP (or $\sigma+$) light results in interband transition (from m_j = -1/2 to +1/2) between the right branches (k_x>0), whereas the absorption of LCP (or $\sigma-$) light allows transition (from m_j = +1/2 to -1/2) between the left branches (k_x<0). Therefore the circularly polarized light creates non-equilibrium spin polarization among the two Rashba branches. Through the inverse Rashba-Edelstein effect [39], a CPGE photocurrent, J_{x+}^C (J_{x-}^C) is generated when the excited-state electrons (holes) relax to the CB (VB) minimum (maximum). Since the group velocity $d\varepsilon/dk_x$ of electrons are opposite in direction and equal in magnitude along k_x, J_{x+}^C and J_{x-}^C are opposite in directions (and similarly for the holes in the splitted VB). We note that the CPGE current is ultrafast via the momentum

scattering that randomizes **k** and, in turn also **S,** since **k** and **S** vectors are locked together in a Rashba splitting situation. Therefore, there is associated terahertz (THz) radiation from the resulting time-varying current [35]. At steady state conditions, the continuous generation of spin-polarized free carriers leads to a continuous-wave (cw) photocurrent that is sensitive to the polarization status of excitation light [30,35,36]. Since the group velocity of free carriers at the bottom (top) of CB (VB) is zero (**Fig. 1D**), which consequently results in null photocurrent in the absence of bias, the CPGE is zero at/below the IB absorption onset. Importantly, CPGE does not exist if the CB and VB possess spin ½ Kramer's degeneracy, since the photoinduced **k**-vector of both LCP and RCP is the same, and thus the group velocity (and photocurrent) does not change direction when the angle α is changed via the QWP rotation.

In addition to the CPGE current associated with circularly polarized light, there is also spin-independent photocurrent when the excitation light is linearly polarized (LP, for α=n(π/2)) [30]. This is known as linear photogalvanic effect (LPGE). Through a 360^0 rotation of the QWP, the incident light polarization cycles through LP, RCP, LP, LCP, and therefore the measured photogalvanic effect (PGE) current, $J_{x'}(\alpha)$ contains both CPGE and LPGE current given by:

$$J_{x'}(\alpha) = C1\sin(2\alpha) + C2\cos(2\alpha) + L1sin(4\alpha) + L2cos(4\alpha) + D. \quad (1)$$

Where x' indicates the measurement direction in **Figure 1C**. The 4α terms describe LPGE, the 2α terms stand for CPGE, and D represents a polarization-independent offset that originates from other effects such as photothermal, photovoltaic response, or photo Dember effect [30,35,36,40]. The cosine term, *C2* is mainly due to misalignment (about 1~ 3 degree, in our case) between the fast axis of the λ/4 waveplate and the incident light polarization, so that *C2*<<*C1*. The relative strengths of LPGE parameter pairs (*L1*, *L2*) depend on several experimental conditions and symmetry tensor (see SM11 in **SI**, and **Auxiliary Supplementary Materials**). In our measurements we found that *L1*<< *L2* (see Supplementary Table **2&4** in **SI**). We note that the coefficients *C1* (for CPGE) and *L2* (for LPGE) depend on the incident angle, θ and azimuthal angle, ϕ' (defined in **Figure 1C**), as detailed in SM5&9 in **SI**. In general, *C1* and *L2* are related to a second order tensor, γ_{ij}, and third order tensor, χ_{ijk}, respectively [30]. The point group symmetry for the triclinic 2D-PEPI is C_i [19,25,26]. Our calculation shows that the inversion symmetry is broken along *z*-axis (out-of-plane) and the crystal *b*-axis (in-plane) (**Figure 1C**). There are three non-zero components for γ_{ij} tensor in C_i, two are in-plane (γ_{xy} *and* γ_{yx}), and one is out-of-plane, γ_{xz} . For χ_{ijk}, there are five non-zero components: $\chi_{xxy}, \chi_{xxz}, \chi_{yxx}, \chi_{yyy}, \chi_{yyz}$. (see SM11 in **SI,** and **Auxiliary Supplementary Materials** for details).

Figure 2A shows the room temperature PGE(α) response [$J_{x'}(\alpha)$] in 2D-PEPI single crystal at steady state conditions and incident angle $\theta=35^0$, using a xenon lamp excitation at 2.30 eV for EX generation, and 2.64 eV for IB excitation, respectively. The *C1*, *L2* and *D* parameters are obtained from fitting using Equ.(1), and seen as colored bars (**Figure 2A** inset). This procedure was repeated for various incident (θ) and azimuthal (ϕ') angles, as well as excitation energies (ω), in order to obtain the complete PGE response of the 2D-PEPI crystal. As is clearly seen, both CPGE (*C1*) and LPGE (*L2*) have opposite signs for resonant excitation at the EX and IB

transitions. This difference in PGE is further illustrated in **Figure 2B,** where the CPGE action spectrum, *C1(ω)* of the 2D-PEPI crystal is displayed (black symbol). It is seen that *C1(ω)* has two spectral regions that are separated at ~2.40 eV; $\hbar\omega$ <2.40 eV for photogenerated excitons and $\hbar\omega$ >2.40 eV for excited state photocarriers generated via IB transition. The CPGE action spectrum for the IB transition (CPGE-IB) is very broad with a maximum at ≈2.52±0.03 eV, whereas the CPGE spectrum related to EX transition (CPGE-EX) consists of a sharp peak at 2.34±0.02 eV and negative valley at 2.30±0.02eV, with a split of ~40 meV, reminiscence of EX1 and EX2 in the reflectivity spectrum of 2D-PEPI (**Figure 1B inset)**. The uncertainty comes from the reduced spectral resolution of the setup (see SM2 in **SI**). In addition, CPGE-IB has associated terahertz (THz) emission, whereas THz emission is not observed when resonantly exciting the excitons with similar photon density ($\sim 4 \times 10^{17}\ photons \cdot cm^{-3}$) (see **Figure 3B** & **3C** below**)**. This shows that the CPGE-IB is in fact ultrafast, whereas the CPGE-EX is not. This indicates that the CPGE-EX current decays (or generated) much slower than sub-picosecond timescale (limit of our setup), and therefore it does not generate THz emission (see below).

Figure 2B also shows the calculated CPGE-IB action spectrum (red line) using a model system consisting of J=½ states for the CB and S=½ states for the VB. The model describes the band edge states in 2D-PEPI crystal and accommodates a Rashba term (see SM12 in **SI**). The key result from our model calculation is that the CPGE-IB spectrum is peaked at energy, E_d that corresponds to the direct transition at k=0 between the Dirac points in the CB and VB (see **Figure 1D**). CPGE-IB has a threshold energy at $E_d - (m_c^* + m_v^*)\,(\alpha_c + \alpha_v)^2/(2\hbar^2)$, where $\alpha_{c(v)}$ is the Rashba coefficient of the CB (VB), and $m_{c(v)}^*$ is the effective mass of the CB (VB). Note that the Rashba splitting energy, E_R corresponds to the energy difference between the threshold and maximum of the CPGE-IB action spectrum, i.e., $E_R = (m_c^* + m_v^*)\,(\alpha_c + \alpha_v)^2/(2\hbar^2)$. **Figure 2B** shows that the experimental CPGE-IB action spectrum is well reproduced by this model, using Rashba splitting of 35±10 meV and broadening parameters of 30±10 meV (details in SM12 in **SI**). The good agreement with the experimental data validates the Rashba splitting in 2D-PEPI continuum bands.

In order to experimentally identify the symmetry breaking axis in 2D-PEPI crystal that leads to the Rashba splitting, we measured the incident angle (θ) dependence of the PGE(θ) response at 2.58 eV (IB) (**Figure 2C**) and 2.30 eV (EX) (**Figure 2D**) at azimuthal angle ϕ'=90^0. For the CPGE-IB in this special case $C1(\theta) = A\sin(\theta) + B\cos(\theta)$, whereas $L2(\theta) = A'\sin(2\theta) + B'\cos(2\theta) + G$. A, B, A', B' and G are fitting parameters with details given in SM11 in **SI**. The dashed lines in **Figure 2C** show the fitting results. The satisfactory fitting for *L2(θ)* with this model proves that the break of inversion symmetry exists along the z-axis (out-of-plane) and crystal b-axis (within the $[PbI_6]^{4-}$ plane) (**Fig. 1C**). The fitting for *C1(θ)* is not as good and yields near zero γ_{xz}, meaning that CPGE mostly results from inversion symmetry breaking along the out-of-plane z-direction. Indeed, *C1* changes sign when θ is reversed, and passes through zero at $\theta = 0^0$. This is due to the coincident line-up of the photocurrent direction (x') in this device with the crystal b-axis (within the $[PbI_6]^{4-}$ plane). Since the inversion symmetry is also broken along b-axis, a null CPGE is

expected if measured in this direction [30]. Non-zero *C1* was observed at normal incidence when the measurement direction was not lined up with *b*-axis (see Supplementary **Table 4**). Details of the fitting analysis can be found in SM11 in **SI**.

Terahertz (THz) emission due to ultrafast photogalvanic (PGE) currents in 2D-PEPI crystal

For demonstrating the instantaneous generation of the PGE response at the IB excitation, we have also used transient THz emission spectroscopy to complement the steady state measurements. **Figure 3A** is a schematic illustration of the experimental set-up for the helicity dependent THz emission measurement. This setup is similar to the one used for the steady state measurements (see **Figure 1C**), except that the crystal is devoid of gold electrodes, hence eliminating related field effect artifacts. The 2D-PEPI crystal is excited with ~ 50 femtosecond (fs) second-harmonic pulses at 3.06 eV using an amplified Ti-sapphire laser operating at a center wavelength of 810 nm, and the THz emission is collected in transmission geometry (see SM9 in **SI**). **Figure 3B** shows the time domain waveforms at three different rotation angles (α) of the QWP measured at normal incidence. The detection electro-optic crystal and a wire grid polarizer were used to measure the emitted field in the *y'*-direction (with angle ψ to the *b*-axis, see **Figure 1C**). The absence of sign reversal for the emission field between RCP ($\alpha = 45^0$) and LCP ($\alpha = 135^0$) can be explained by the presence of in-plane inversion symmetry breaking, similar as observed in [30], consistent with the measurement in **Figure 2C**.

Figure 3C shows the THz field emission vs. α at incident angle $\theta = 45^0$. The data points for the **E**-Field are extracted as 'peak-to-peak' values in the THz emission signal (see the broken lines in **Figure 3B**). The peak-to-peak value of the **E**-field corresponds to the amplitude of the PGE current, *J*, as defined in the phenomenological model described in Equ. (1). The red line is a fit using Equ. (1). The lower inset shows the obtained relative values of the coefficients *C1*, *L2* and *D*. It is clearly seen that the THz emission intensity depends on the pulsed light polarization helicity, similar to the steady state results in **Figure 2A**, and has a strong *sin(2α)* component that originates from CPGE. Ultrafast current is known to result in pulsed THz emission that corresponds to sub-picosecond electric field, and the THz emission is proportional to the time derivative of the photocurrent. Since the duration of the pulse excitation is ~50 fs in our THz setup, the relatively strong THz emission here indicates that the polarized photocurrent is very short lived. This is consistent with the process of PGE current that is estimated to happen in the femtosecond time domain, associated with momentum scattering time of the material, as described in **Figure 1D**. We note that THz emission associated with fast PGE current has been presented in previous studies [35,41-42]. We also conclude that the THz emission is unlikely to originate from optical phonons, as such process would have a different characteristic transient; namely long-lived periodically modulated signal [43, 44] rather than a single cycle emission as measured in **Figure 3B**. In fact, we measured the optical phonon modes using terahertz transmission through the crystal w.r.t. to reference substrate. Phonons in 2D-PEPI can be observed at 0.78 THz and 1.6 THz, respectively (see **Supplementary Figure 12** in **SI**); probably associated with Pb-I-Pb rocking vibration and Pb-I stretching modes [43]. Moreover, the helicity

dependence of the THz emission points to a spin-dependent process, which is also present in CW measurements, rather than simply due to phonons.

We also measured substantial ultrafast LPGE component (see **Supplementary Figure 13**) at normal incidence indicating that this linear PGE effect is due to 'shift current', caused by the displacement of the electron charge center upon undergoing a transition from the VB to CB [45] (see SM9 in **SI**). **Figure 3D** shows similar measurements as in **Figure 3C** but at normal incidence ($\theta = 0^0$). The extracted parameters show much smaller contribution of *C1* at normal incidence, in agreement with the CW measurements (**Figure 2C**). We note in passing that an important difference exists between the THz and steady state measurements, which is the much-reduced contribution of the THz emission associated with the background current *D* (see inset of **Figure 3C**). It is conceivable that *D* in THz emission mainly comes from the (ultrafast) photo-Dember effect [44], whereas in CW excitation slow processes, such as photothermal effect dominate [40].

In contrast to the spectral response of CPGE-IB, the spectrum of CPGE-EX has a completely different line shape (**Figure 2B,** left of the broken line). Here the action spectrum comprises of a derivative-like feature with a negative valley at 2.30 eV and peak at 2.34 eV; however it is not the first derivative of the absorption. Furthermore, upon 180^0 rotation of the device the derivative-like feature converges into a single band (see **Supplementary Figure 3** in **SI**). Also, as shown in **Figure 2A**, the PGE(α) response at the exciton photon energy is very different from that at the interband. In addition, the incident angle θ–dependence of both CPGE (*C1*) and LPGE (*L2*) at the exciton energy (**Figure 2D**) are also very different from those at the interband (**Figure 2C**). In fact, for the exciton excitation, $C1 \neq 0$ at $\theta = 0^0$, and *L2* is almost zero at negative θ angle. Importantly, no THz emission related to the CPGE-EX was observed (see **Figure 3B** inset), indicating a slower dynamic of the helicity dependent photocurrent generated from the exciton dissociation. Furthermore, the sense of spin is opposite at the valley and peak of the CPGE-EX spectrum. We thus conclude that the spin-dependent photocurrent associated with the photogenerated excitons is a feature that cannot be explained by the CPGE traditional band model [30, 35, 36].

Clearly the excitons in 2D-PEPI substantially contribute to the photocarriers density (see photoconductivity action spectrum in **SI**, **Supplementary Figure 4**). Although the PGE current was measured at zero bias, at steady state there is still a small electric field (estimated to be about 500V/cm, see SM5 in **SI**) within the device that originates from the photothermal effect due to light-induced temperature gradient across the device and/or photovoltaic effect from slight asymmetry between the two Au electrodes [35, 40]. This weak electric field contributes to the DC offset current *D* (see MM5 in SI). However, based on our calculation, this weak electric field is not strong enough to dissociate the excitons in 2D-PEPI because of the large exciton binding energy here (>250 meV) [24, 29, 37]. Yet, as shown in ref. [46], efficient exciton dissociation may occur at native defects in the crystal. We also note that the exciton CPGE occurs below the exciton main absorption, and that the CPGE (*C1*) current polarity depends on the incident angle θ (**Figure 2D**).

One possible mechanism to explain these puzzling results is that the helicity dependent photocurrent at the exciton band is in fact due to the spin-galvanic effect (SGE) rather than the CPGE. In this scenario the spin angular momentum of the impinging light is conserved during the absorption by the exciton. To verify this assumption we have measured a transient circular polarization memory at the exciton level at RT using the transient polarized photoinduced absorption technique at 537 nm with 150 fs time resolution. In this method we set the pump beam polarization at a fix circular polarization, whereas the circular polarization of the probe beam was modulated between same circular polarization or opposite polarization to that of the pump beam (see SM10 in **S.I**. for detail). In this method only the difference between the same or opposite pump-probe circular polarizations is measured. Firstly, we found that there is 'circular polarization memory' for the exciton, in which the photoinduced absorption is larger when the pump-probe have same polarization compared to that of pump-probe with opposite polarization (see **Supplementary Figure 16** in SM10, **SI**). This shows that the excitons are spin polarized following excitation by a circularly polarized pump. Secondly, we measured the RT circular polarization lifetime, or spin relaxation time to be ~4.5 ps on the average (see **Supplementary Figure 17** in SM10, **SI**). Subsequently, some of the spin polarized excitons dissociate into spin polarized electron-hole pairs that contribute to the photocurrent. The exciton dissociation process may be via edge states, or other native defects in the 2D-PEPI crystal. Since the continuum bands in 2D-PEPI are spin splitted due to the Rashba interaction, therefore the exciton-related spin polarized carriers preferentially occupy one spin sub-band over the other, depending on the light beam helicity. This non-equilibrium spin occupancy causes asymmetric spin-flipping between the two spin sub-bands and results in a current flow in the MQW plane. This situation has been known in the literature as spin-galvanic effect (SGE) [47,48]. A similar situation occurs in the Rashba-Edelstein effect upon spin injection from a ferromagnet electrode [49], except that in our case the spin injection occurs by optical means. The SGE in our case is not ultrafast, since it takes some time for the excitons to dissociate at native defects in the crystal. In addition, the spin relaxation time is not in the sub-ps time domain. These explain the lack of THz emission due to the SGE of the excitons in 2D-PEPI.

Discussion

Using circularly polarized light excitation we obtained steady state spin dependent photocurrent and ultrafast terahertz (THz) emission, which verify the existence of CPGE in 2D-PEPI single crystal multiple quantum wells (MQW). The circular photogalvanic effect (CPGE) action spectrum contains two distinct features that are due to excitons and free carriers, respectively. The CPGE at the interband excitation is a 'smoking gun' proof for Rashba splitting in the continuum bands of 2D-PEPI, which is caused by the large SOC and structural inversion symmetry breaking. We found that the main axis of inversion symmetry breaking is perpendicular to the MQW planes, but there is also small contribution from in-plane inversion asymmetry. In contrast, the spin dependent photocurrent upon exciton excitation is caused by spin-galvanic effect, which also proves the occurrence of Rashba splitting in 2D-PEPI. Our

findings highlight the importance of excitons for helicity dependent photocurrent in 2D perovskites MQW, a topic that has not been properly dealt with in the well-established CPGE theory in semiconductor MQW.

Methods

Samples preparation. PbI_2, R-NH_3I (where R is $C_6H_5C_2H_4$), N,N′-dimethylformamide (DMF), g-butyrolactone (GBL), and dichloromethane (DCM) were purchased from Sigma-Aldrich Corporation. All the materials were used as received without further purification.

All samples were fabricated in a nitrogen-filled glove box with oxygen and moisture levels of <1 part per million. We have grown the 2D hybrid perovskite (2D-PEPI) single crystals on cleaned quartz substrates using the Anti-solvent Vapor-assisted Crystallization (AVC) method as in ref. [1]. The 2D-PEPI crystals were used for the following measurements: photoluminescence (PL) spectrum, terahertz emission spectroscopy, XRD and SEM microscopy. For the device used in continuous-wave (CW) PGE measurement, two 70 nm thick gold electrodes were deposited onto the crystal by e-beam evaporation through a shadow mask in a glove-box-integrated vacuum deposition chamber (Angstrom Engineering), which had a base pressure of 3×10^{-8} torr ($\approx 4 \times 10^{-6}$ Pa). The gap between electrodes was 0.5 mm.

For the solution used to create 2D-PEPI film, we mixed R-NH_3I and PbI_2 in a 2:1 molar ratio in DMF solvent to form a solution with a concentration of 0.2 mol/ml. This solution was stirred overnight at 60 ℃ on a hotplate before using. Subsequently the solution was spin-coated on an oxygen plasma–pretreated glass substrate at 314 rad/s and 90 s to form 100 nm thick film; the obtained film was subsequently annealed at 100 °C for 30 min. We used this film for the optical density measurement.

Continuous wave (CW) PGE measurement. CW diode lasers that operate at wavelengths of 405 nm, 447 nm, 486 nm, 520 nm and 532 nm, respectively were used to excite the 2D-PEPI single crystal between the two gold electrodes of the device. The laser beam with a diameter of 0.25 mm to 0.45 mm was focused exactly at the center between the two electrodes to minimize the effects caused by electrode asymmetry. In these measurements, the laser power was reduced to 45 μW, with a diameter of 0.35 mm, so that the light intensity was 31 mW/cm^2. For measuring the CPGE action spectrum, we also used as a pump excitation an incandescent light source from a xenon lamp, which was dispersed through a monochromator. Roughly 25 % of the light beam was focused on the active area of the device, with an area 0.5 mm x 0.75 mm, with an intensity of 8.0 mW/cm^2. Due to the very low intensity of Xenon lamp, we use full-slit width of the monochromator to ensure the needed intensity for measurable signal.

Photoconductivity action spectrum. In this measurement, the incandescent light from a Xe lamp, which was dispersed through a monochromator, was used to excite the same device used in the CPGE measurement. We also measured the conductivity by sweeping the voltage applied to the device with a Keithley 238 multimeter. The voltage was swept in a symmetrical way (0 V

to -5 V, +5V to -5 V, -5V to 0 V). The photoconductivity was then subtracted by linearly fitting the I-V curve from +5 V to -5 V. This procedure was adopted from ref. [36].

Terahertz emission measurements. Terahertz emission from 2D-PEPI crystals was measured by an electro-optic sampling technique using standard time-domain spectroscopy configuration. The samples were excited by 0.25 μJ pulses at 405 nm generated using type-I BBO crystal pumped with 810 nm pulses from Ti-Sapphire regen-amplified laser system at 1 KHz repletion rate. 2D-PEPI crystals on Quartz substrate were excited from the quartz side. The emitted terahertz radiation due to photo-excited carriers was collected by 2 parabolic mirrors and focused on to 0.5 mm thick electro-optic ZnTe <110> crystal. The terahertz field pulse signal was measured as the change in polarization of the probe beam induced as a result of electro-optic sampling technique, as measured by a Wollaston prism and a set of balanced silicon detectors using lock-in technique. We note that the measured bandwidth of the emitted signal detection technique is limited by the detection crystal. To measure the polarization dependent terahertz field, the sample was mounted on a rotation stage and the excitation beam was modulated using $\lambda/2$ and $\lambda/4$ plate. In addition, a wire grid polarizer was placed in the collimated beam path between the two parabolic mirrors, to allow detection of polarization emitted terahertz field.

Optical characterizations

All optical measurements were done at room temperature in air. The absorption (or optical density) was measured using a UV/Vis spectrometer (Olis). For the photoluminescence (PL) measurement, a 2D-PEPI single crystal was excited using a 30 mW CW laser at 486 nm. The reflectivity spectrum from 2D-PEPI crystal was measured using Woollam variable angle spectroscopic ellipsometer (VASE) on large area crystals grown on quartz substrates with average thickness 8 to 13μm. The equipment has built-in setup for reflectivity measurement of s-polarized and p-polarized light.

Data availability

The data that support the findings of this study are available from the corresponding

author upon reasonable request.

Code availability

We have included the original code for calculation of symmetry tensor as additional supporting material (auxiliary supporting material). The algorithm for band model calculation are available from the corresponding author upon reasonable request.

References

1. Eames, C. *et al.* Ionic transport in hybrid lead iodide perovskite solar cells', *Nature Comm* **6**, 7497-7505 (2015).

2. Miyata, A. *et al.* Direct measurement of the exciton binding energy and effective masses for charge carriers in organic–inorganic tri-halide perovskites. *Nature Physics* **11**, 582-588 (2015).
3. Hutter, E.M., Gélvez-Rueda, M. C., Osherov, A., Bulovic, V., Grozema, F. C. Direct–indirect character of the bandgap in methylammonium lead iodide perovskite. *Nature Materials* **16**, 115-121 (2016).
4. Stranks, S.D. *et al.* Interface engineering of highly efficient perovskite solar cells. *Science* **345**, 542 (2014).
5. Nie, W. *et al.* High-efficiency solution-processed perovskite solar cells with millimeter-scale grains. *Science* **347**, 522-525 (2015).
6. Arora, N. *et al.* Perovskite solar cells with CuSCN hole extraction layers yield stabilized efficiencies greater than 20%. *Science* **358**, 768–771 (2017).
7. Wang, J. *et al.* Interfacial Control Toward Efficient and Low-Voltage Perovskite Light-Emitting Diodes. *Adv. Mater*. **27**, (2311–2316) 2015.
8. Sutherland B. R., Sargent, E.H. Perovskite photonic sources. *Nature Photonics* **10**, 295-302 (2016).
9. Veldhuis, S. A. *et al.* Perovskite Materials for Light-Emitting Diodes and Lasers. *Adv. Mater.*,**28**, 6804–6834(2016).
10. Bychkov Y. A., Rashba, E.I. Properties of 2D electron gas with lifted spectral degeneracy. *JETP Lett*. **39**, No. 2, (1984).
11. Etienne, T., Mosconi, E., De Angelis, F. Dynamical Origin of the Rashba Effect in Organohalide Lead Perovskites: A Key to Suppressed Carrier Recombination in Perovskite Solar Cells?. *J. Phys. Chem. Lett*. **7**,1638 (2016).
12. Zheng, F., Tan, L.Z., Liu, S., Rappe, A.M. Rashba Spin–Orbit Coupling Enhanced Carrier Lifetime in $CH_3NH_3PbI_3$. *Nano Lett.* **15(**12):7794 (2015).
13. Frohna, K. *et al.* Inversion symmetry and bulk Rashba effect in methylammonium lead iodide perovskite single crystals. *NATURE COMMUNICATIONS* | (2018) **9**:1829.
14. Stranks S. D., Plochocka, P. The influence of the Rashba effect. *Nature materials* **17**, 381-382 (2018).
15. Kepenekian, M. *et al.* Rashba and Dresselhaus Effects in Hybrid Organic Inorganic Perovskites: From Basics to Devices. *ACS Nano* **9**, 11557-11567 (2015).
16. Zhang, C. *et al.* Magnetic Field Effect in Hybrid Perovskite Devices. *Nature Physics* **11**, 427-434 (2015).
17. Wang, J. *et al.* Spin-optoelectronic devices based on hybrid organic-inorganic trihalide perovskites. *Nature Communications* (2019) **10**:129.
18. Stoumpos, C.C, Ruddlesden−Popper Hybrid Lead Iodide Perovskite 2D Homologous Semiconductors, Chem. Mater. 2016, 28, 2852−2867.
19. Du, K. et al., Two-Dimensional Lead(II) Halide-Based Hybrid Perovskites Templated by Acene Alkylamines: Crystal Structures, Optical Properties, and Piezoelectricity, Inorg. Chem. 2017, 56, 9291−9302.
20. Misra, R. K., Cohen, B., Iagher, L., Etgar, L. Low-Dimensional Organic–Inorganic Halide Perovskite: Structure, Properties, and Applications. *ChemSusChem* **10**, (3712 – 3721)2017.
21. Even, J., Pedesseau, L., Katan, C. Understanding Quantum Confinement of Charge Carriers in Layered 2D Hybrid Perovskites. *ChemPhysChem* **15,** 3733 – 3741(2014).
22. Kenichiro Tanaka & Takashi Kondo, Bandgap and exciton binding energies in lead iodide-based natural quantum-well crystals, Science and Technology of Advanced Materials 4 (2003) 599–604.
23. Calabrese, J. et al. Preparation and Characterization of Layered Lead Halide Compounds. J. Am. Chem. Soc. 113, (2328-2330)1991.
24. Fang, H-H. *et al.* Unravelling Light-Induced Degradation of Layered Perovskite Crystals and Design of Efficient Encapsulation for Improved Photostability. *Adv. Funct. Mater.* **28,** (1800305-1800316)2018.
25. Fieramosca, A. *et al.* Tunable Out-of-Plane Excitons in 2D Single-Crystal Perovskites. *ACS Photonics* **5**, 4179−4185(2018).
26. Yin, J. et al., Layer-Dependent Rashba Band Splitting in 2D Hybrid Perovskites, Chem. Mater. 2018, 30, 8538−8545.
27. A. J. Morris and B. Monserrat, Optical absorption driven by dynamical symmetry breaking in indium oxide, Phys. Rev. B (rapid comm), vol. 98 161203(R) (2018).
28. Zhai, Y. *et al.*, Giant Rashba splitting in 2D organic-inorganic halide perovskites measured by transient spectroscopies, *Sci. Adv.* **3**: e1700704 (2017).

29. Chen, X. *et al.*, Impact of Layer Thickness on the Charge Carrier and Spin Coherence Lifetime in Two-Dimensional Layered Perovskite Single Crystals, ACS Energy Lett. 2018, 3, 2273−2279.
30. Ganichev, S. D., Prettl, W. Spin photocurrents in quantum wells. *J. Phys. Condens. Matter* **15**(20):R935 (2003).
31. Thouin, F. *et al*., Phonon coherences reveal the polaronic character of excitons in two-dimensional lead halide perovskites, Nature Materials **18**, 349–356 (2019).
32. Lechner, V. *et al.* Spin and orbital mechanisms of the magnetogyrotropic photogalvanic effects in GaAs/AlxGa1−xAs quantum well structures. *Phys. Rev. B* **83**(15):155313 (2011).
33. J. S. Lee, G. A. H. Schober, M. S. Bahramy, H. Murakawa, Y. Onose, R. Arita, N. Nagaosa, and Y. Tokura1, Optical Response of Relativistic Electrons in the Polar BiTeI Semiconductor, PRL 107, 117401 (2011).
34. Yuan H, Wang X, Lian B, Zhang H, Fang X, Shen B, Xu G, Xu Y, Zhang SC, Hwang HY, Cui Y, Generation and electric control of spin–valley-coupled circular photogalvanic current in WSe_2. Nat. Nanotechnol. 9(10):851(2014).
35. McIver JW, Hsieh D, Steinberg H, Jarillo-Herrero P, Gedik N, Control over topological insulator photocurrents with light polarization. Nat. Nanotechnol. 7(2):96 (2012).
36. Obraztsov, P. A. et al. Ultrafast zero-bias photocurrent and terahertz emission in hybrid perovskites. COMMUNICATIONS PHYSICS | (2018) 1:14.
37. Niesner, D. et al. Structural fluctuations cause spin-split bands in (CH3NH3)PbI3: Experimental evidence from circular photogalvanic effect. PNAS, 115, no. 38, 9509–9514(2018).
38. Li, J., Haney, P.M. Circular photogalvanic effect in organometal halide perovskite $CH_3NH_3PbI_3$. *Appl. Phys. Lett.* **109**(19):193903 (2016).
39. V.M. Edelstein, Spin polarization of conduction electrons induced by electric field in two-dimensional asymmetric electron systems, Solid State Comm. 73, 233-235 (1990)
40. Osterhoudt, G. B. *et al.* Colossal mid-infrared bulk photovoltaic effect in a type-I Weyl semimetal', *Nature Materials* **18**, 471–475 (2019).
41. Kinoshita, Y., Kida, N., Miyamoto, T., Kanou, M., Sasagawa, T. and Okamoto, H., 2018. Terahertz radiation by subpicosecond spin-polarized photocurrent originating from Dirac electrons in a Rashba-type polar semiconductor. Physical Review B, 97(16), p.161104.
42. Sirica, N., Tobey, R.I., Zhao, L.X., Chen, G.F., Xu, B., Yang, R., Shen, B., Yarotski, D.A., Bowlan, P., Trugman, S.A. and Zhu, J.X., 2019. Tracking ultrafast photocurrents in the Weyl semimetal TaAs using THz emission spectroscopy. Physical review letters, 122(19), p.197401.
43. M. Sender *et al.*, Optical phonons in methylammonium lead halide perovskites and implications for charge transport, Materials Horizons 3, 613-620 (2016).
44. Guzelturk, B. *et al*., Terahertz Emission from Hybrid Perovskites Driven by Ultrafast Charge Separation and Strong Electron–Phonon Coupling, Adv. Mater. 2018, 30, 1704737.
45. Vikhnin, V.S., Eglitis, R.I., Kapphan, S.E., Borstel, G., Kotomin, E.A., Polaronic-type excitons in ferroelectric oxides: Microscopic calculations and experimental manifestation. *PHYSICAL REVIEW B*, **65**, 104304 (2002).
46. Blancon, J.-C *et al.* Extremely efficient internal exciton dissociation through edge states in layered 2D perovskites. Science **355**, 1288–1292 (2017).
47. Ganichev, S.D. *et al.*, Spin-galvanic effect, Nature 417, 153 (2002).
48. Götz Seibold, Sergio Caprara, Marco Grilli, and Roberto Raimondi, Theory of the Spin Galvanic Effect at Oxide Interfaces, Phys. Rev. Lett. **119**, 256801(2017).
49. J.C. Rojas Sánchez J.C. R. et al., Spin-to-charge conversion using Rashba coupling at the interface between non-magnetic materials, *Nat. Comm*. **4**, 2944 (2013).

Acknowledgments

The CW CPGE measurements were supported by the Department of Energy Office of Science, Grant DESC 0014579. The crystal growth facility, the optical and morphological characterizations, and the transient circular polarization measurements were supported by the Center for Hybrid Organic-Inorganic Semiconductors for Energy (CHOISE), an Energy Frontier Research Center funded by the Office of Basic Energy Sciences, Office of Science within the US

Department of Energy. The CPGE THz emission studies were supported by the NSF grant EECS 1810096. F.X. acknowledges support under the Cooperative Research Agreement between the University of Maryland and the National Institute of Standards and Technology Physical Measurement Laboratory, Award 70NANB14H209, through the University of Maryland. We also thank Dr. Pete Sercel for fruitful discussion.

Author contributions

X.L. synthesized and grew the 2D-PEPI crystals and fabricated the devices used in this work. X.L. also conducted the CW CPGE measurements and optical characterizations (absorption, photoluminescence and photoconductivity). A.C. and S. B. conducted the THz measurements; A.C. also did all structural characterizations (XRD, SEM, AFM). X.L. and A.C. conducted the reflectivity measurement. U.H did the transient circularly polarized pump and probe measurement. F.X. and P.M.H. did the modeling and theoretical calculation of symmetry tensors and CPGE action spectrum. P.M.H also provided software programming. X.J and Z.V.V are the correspondent authors of this work. This has included: conceptualization of the study; design and guidance of experiments; and analysis of the data. X.J. wrote the original draft with input from all authors, and Z.V.V. and P.M.H. edited the consequent versions of the manuscript.

Competing interests

The authors have no competing interests.

Figures with Captions

Fig. 1. Rashba splitting in 2D hybrid organic-inorganic perovskite (2D-PEPI) crystal: **A,** Schematic of the 2D-PEPI structure with alternating ($C_6H_5C_2H_4NH_3^+$) and $[PbI_6]^{4-}$ layers, which form natural multiple quantum wells (MQW), where the inorganic layer is the potential 'well' and organic layer is the potential 'wall'. The potential values were taken from ref [22]. The crystal structure is triclinic at room temperature, with growth direction along the c-axis. **B,** Room temperature absorption (black line) spectrum of a thin film 2D-PEPI where the exciton (EX) and interband (IB) transitions are denoted. The inset shows the reflectivity spectrum of a single crystal (blue symbol), having two different spectra features. The red(blue) broken line marks the two exciton species (EX1/EX2) observed in the 2D-PEPI crystal. **C,** Experimental set-up for measuring the PGE using $\lambda/4$ plate; the angles α, θ, and ϕ are denoted. x' indicates the current flow direction, making an angle, ψ with the crystal a-axis. **D,** Schematic diagram of the continuum bands (VB and CB) having Rashba spin splitting, and related optical transitions with circular polarized light. The electron group velocity (and current) change polarity when the light changes helicity. E_d is the direct energy difference between the CB and VB Dirac points.

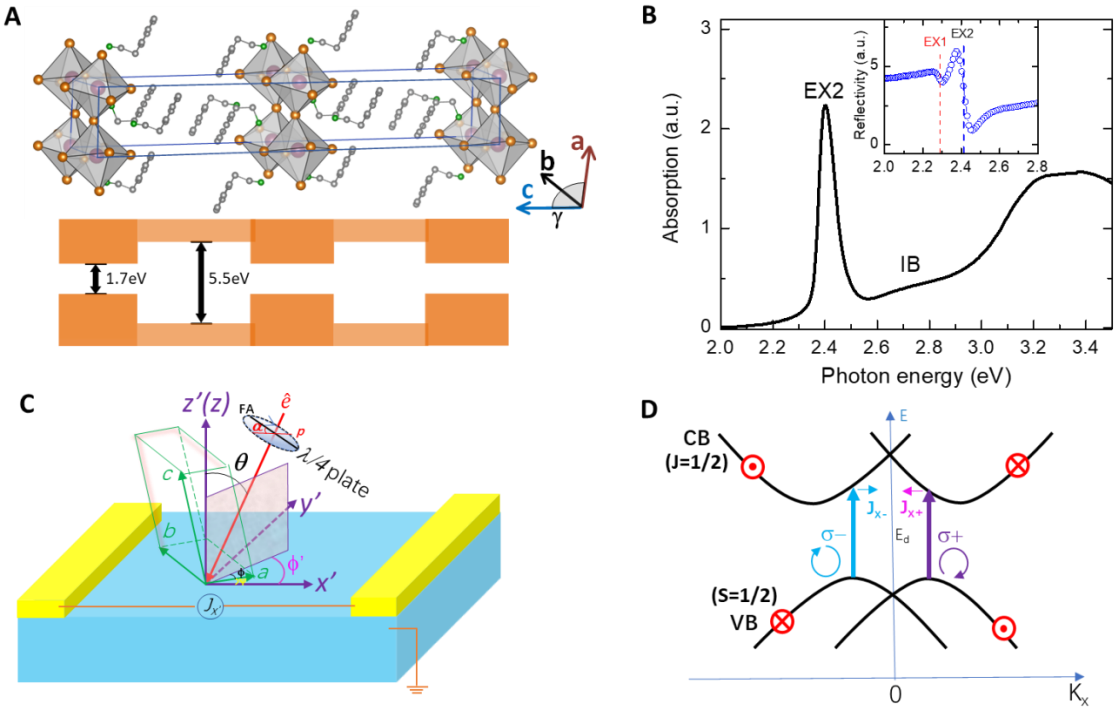
A
a
b
c
γ
1.7eV
5.5eV
B
Absorption (a.u.)
Photon energy (eV)
EX2
IB
Reflectivity (a.u.)
EX1
EX2
C
z'(z)
FA
ê
θ
λ/4plate
c
b
a
y'
x'
ϕ'
J_x
D
E
CB
(J=1/2)
J_{x-}
J_{x+}
σ−
σ+
E_d
(S=1/2)
VB
0
K_x

Fig. 2. Continuous wave (CW) photogalvanic (PGE) currents in 2D-PEPI crystal: **A,** The room temperature photogalvanic current in 2D-PEPI crystal vs. λ/4 plate rotation angle, α measured at θ=30^0, excited at resonance with the exciton (blue squares) and interband (black squares) that is shifted vertically for clarity. The red lines through the data points are fits using Eq. (1) with fitting parameters C1, D and L2 shown in the insets. **B**, The CPGE (C1) action spectrum of 2D-PEPI crystal (black squares); the red line through the data points is a fit using a four bands model (see text). The error bars (cyan, s.e.m.) indicate the uncertainty of special data points close to zero. C1(ω) spectrum is divided by a vertical broken line into two spectral ranges, exciton (EX) and interband (IB). The two exciton species are labeled as EX1 &EX2. **C,** The CPGE amplitude, C1 (blue squares) and LPGE amplitude, L2 (red triangles) vs. the incident angle, θ, at resonant excitation with the interband (IB, at 2.58 eV). The broken lines are fittings (see text). **D**, The incident angle θ dependence of C1 (blue circles) and L2 (red circles) at resonant excitation with the exciton (EX1, at 2.30 eV).

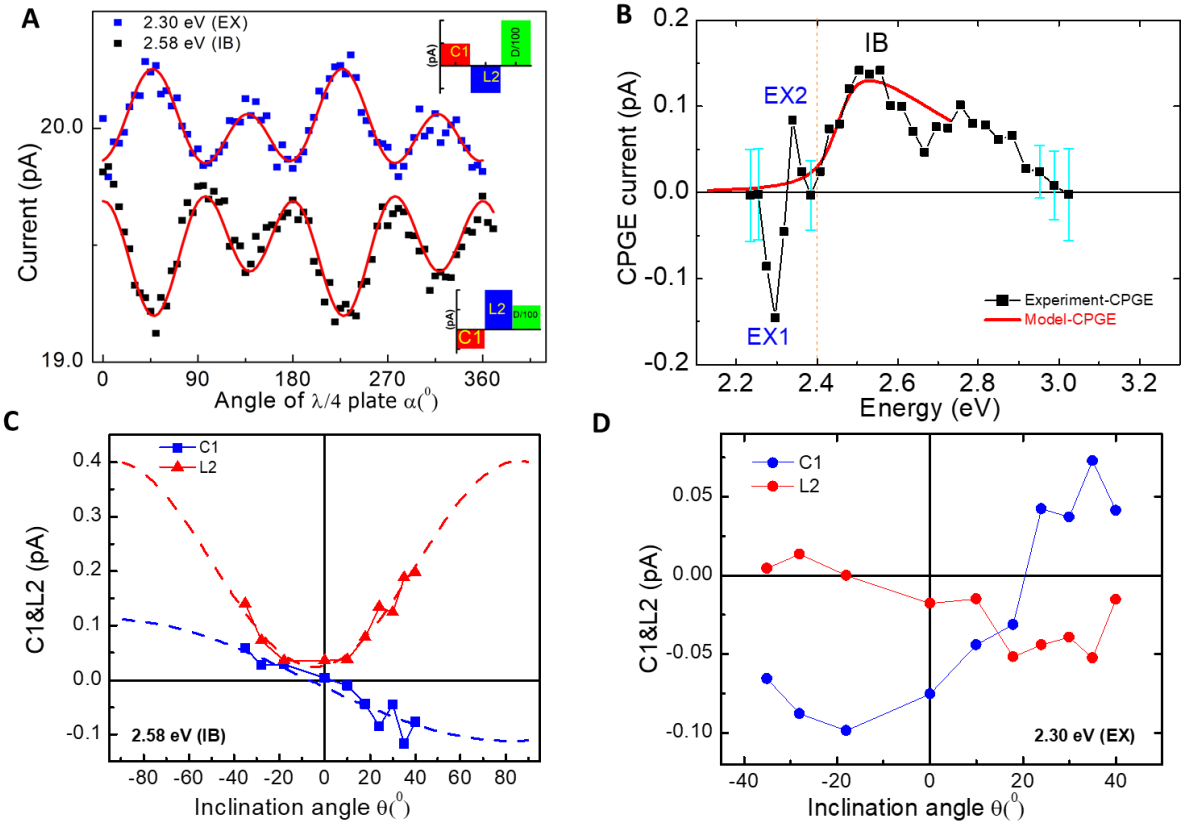

Fig. 3. Terahertz (THz) emission due to ultrafast photogalvanic (PGE) currents in 2D-PEPI crystal:

A, schematic illustration of the experimental set-up for the THz emission measurements. The angles α, θ, and φ are denoted. **B**, THz time domain emission waveforms measured at λ/4 wave plate angle, α, of 0˚, 45˚ and 135˚ as denoted, that correspond to linear polarized (LP), right circularly polarized (RCP) and left circularly polarized (LCP) light. The two dashed black lines mark the times where positive and negative peaks of the terahertz emission were determined. The peak-to-peak values are determined from the addition of the absolute positive and negative values as marked by the dots. The inset shows a null signal obtained when resonantly excited at the exciton band (2.34 eV). **C**. Terahertz field emission vs. the rotation angle, α, photogenerated using 3.06 eV pulsed excitation at θ=45˚. The red line through the black data points is a fit using Eq. (1). The inset shows the obtained relative values of the coefficients C1, L2 and D; D. Similar measurements as in panel C, for incident angle, θ=0˚. The fit using Eq. (1) shows majority contribution from L2. The blue dashed line marks the noise level corresponding to zero emission field.

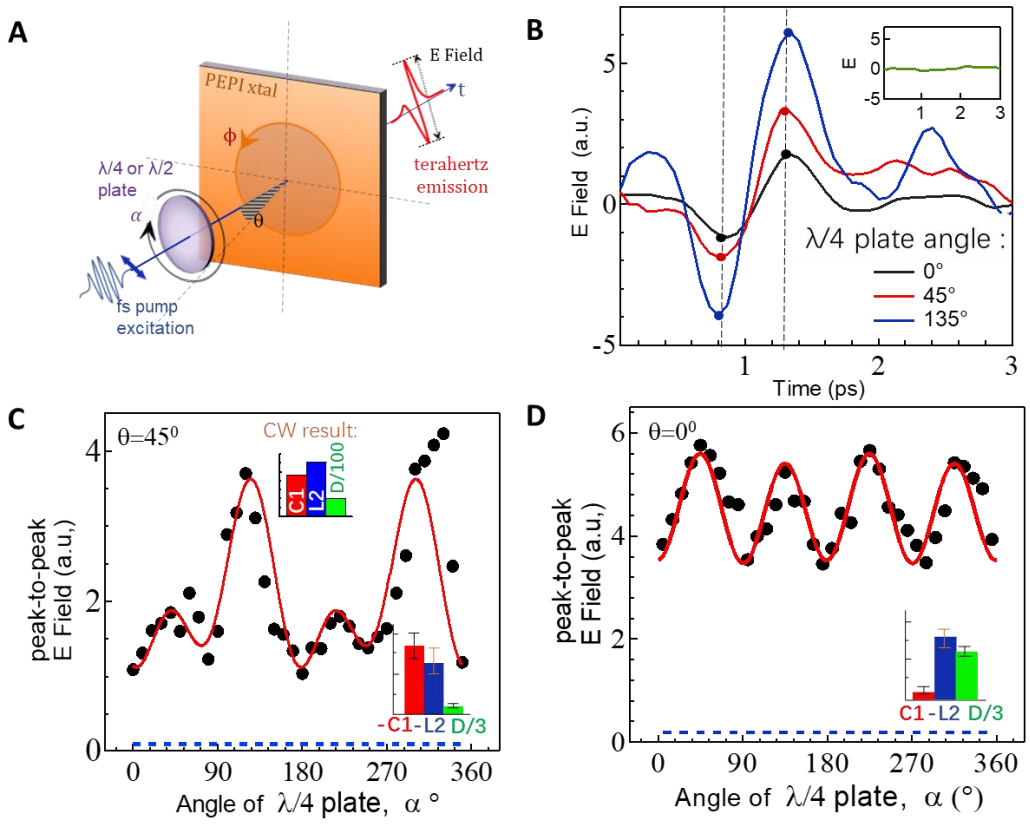

Supplementary Materials

Circular photogalvanic spectroscopy of Rashba splitting in 2D hybrid organic-inorganic perovskite multiple quantum wells

Xiaojie Liu[1], Ashish Chanana[1,2], Uyen Huynh[1], Fei Xue[3,4], Paul Haney[3], Steve Blair[2], Xiaomei Jiang[5*] and Z. V. Vardeny[1*]

[1]: Department of Physics & Astronomy, University of Utah, Salt Lake City, UT 84112, USA

[2]: Department of Electrical Engineering, University of Utah, Salt Lake City, UT 84112, USA

[3]: Center for Nanoscale Science and Technology, National Institute of Standards and Technology, Gaithersburg, MD 20899, USA.

[4]: Institute for Research in Electronics and Applied Physics & Maryland Nanocenter, University of Maryland, College Park, MD 20742, USA

[5]: Department of Physics, University of South Florida, Tampa, FL 33620, USA

1. Supplementary Methods (SM)

SM1. Samples preparation

PbI_2, R-NH_3I (where R is $C_6H_5C_2H_4$), N,N'-dimethylformamide (DMF), g-butyrolactone (GBL), and dichloromethane (DCM) were purchased from Sigma-Aldrich Corporation. All the materials were used as received without further purification.

All samples were fabricated in a nitrogen-filled glove box with oxygen and moisture levels of <1 part per million. We have grown the 2D hybrid perovskite (2D-PEPI) single crystals on cleaned quartz substrates using the Anti-solvent Vapor-assisted Crystallization (AVC) method as in ref. [1]. The 2D-PEPI crystals were used for the following measurements: photoluminescence (PL) spectrum, terahertz emission spectroscopy, XRD and SEM microscopy. For continuous-wave (CW) PGE measurement, two 70 nm thick gold electrodes were deposited onto the crystal by e-beam evaporation through a shadow mask in a glove-box-integrated vacuum deposition chamber (Angstrom Engineering), which had a base pressure of 3×10^{-8} torr ($\approx 4 \times 10^{-6}$ Pa). The gap between electrodes was 0.5 mm. **Supplementary Figure 1 (B)** is a photo of the device.

For 2D-PEPI film we mixed R-NH_3I and PbI_2 in a 2:1 molar ratio in DMF solvent to form a solution with a concentration of 0.2 mol/ml. This solution was stirred overnight at 60 ℃ on a hotplate before using. Subsequently the solution was spin-coated on an oxygen plasma–pretreated glass substrate at 314 rad/s and 90 s to form 100 nm thick film; the obtained film was subsequently annealed at 100 °C for 30 min. We used this film for the optical density measurement.

SM2. Continuous wave (CW) PGE measurements

CW diode lasers that operate at wavelengths of 405 nm, 447 nm, 486 nm, 520 nm and 532 nm, respectively were used to excite the 2D-PEPI single crystal between the two gold electrodes of the device. The laser beam with a diameter of 0.25 mm to 0.45 mm was focused exactly at the center between the two electrodes to minimize the effects caused by electrode asymmetry. In these measurements, the laser power was reduced to 45 μW, with a diameter of 0.35 mm (**Supplementary Figure 1 (A)**), so that the light intensity was 31 mW/cm^2. For measuring the CPGE action spectrum, we also used as a pump excitation an incandescent light source from a xenon lamp, which was dispersed through a monochromator. Roughly 25 % of the light beam was focused on the active area of the device, with an area 0.5 mm x 0.75 mm (**Supplementary Figure 1 (C)**), with an intensity of 8.0 mW/cm^2. **Supplementary Table 1** lists the comparison between actual power and intensity on the device, and **Supplementary Figure 1 (A-C)** shows photos of the device and beam sizes of these two cases. A comparison of PGE current is shown in **Supplementary Figure 1 (D,E)**. A quarter (λ/4) waveplate (QWP) and a half (λ/2) waveplate (HWP or polarizer) were used to modify the polarization property of the exciting light before the sample. In both cases the incident light is p-polarized. The light beam intensity was modulated at a frequency of 310 Hz, and the photocurrent was measured using a lock-in amplifier. Due to the very low intensity of Xenon lamp, we use full-slit width of the monochrometer to ensure the needed intensity for measuable signal. **Supplementary Figure 1 (F)** shows a lineshape of the xeon light after the monochrometer at wavelength of 510nm. This reduced spectral resolution has resulted in ±22-24meV uncertainty in the energy range used in **Supplementary Figure 2(B)**.

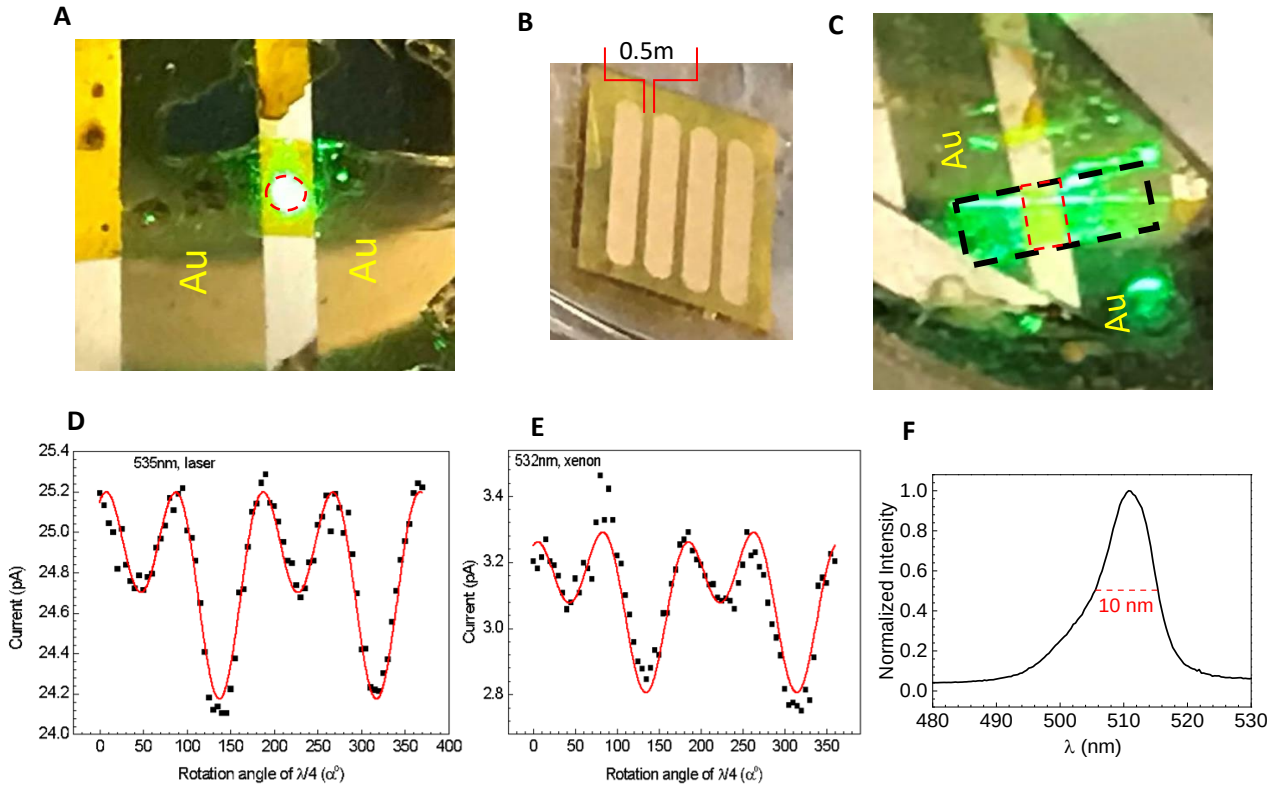

Supplementary Figure 1. (**A**) A photo of the PGE device under laser illumination at 535 nm. The red dashed line outlines the beam size (disk with diameter 0.25 mm). (**B**) Picture of a thin film device showing the device geometry. (**C**) The device under xenon light illumination. The black dashed line shows the full beam size, which is roughly 4x of the beam (0.5 mm x 0.75 mm) on the device (red dashed line). The wide dark bar is the Au electrode, and the narrow bright bar is the crystal. (**D**)-(**E**) PGE current in 2D-PEPI crystal vs. quarter- wave plate angle, α (at $\theta=35^0$), with (**D**) CW excitation of laser, 535 nm, power = 45 μW; and (**E**) xenon lamp, 530 nm, power = 30 μW. The redline is fitting using equ. (1) in main text. The extracted parameters are listed in **Supplementary Table 2**. (**F**) The profile of Xe lamp after the monochromator at 510nm. The full width at half maximum (FWHM) is about 10 nm. So the wavelength error bar for CPGE measurement is ±5nm. The corresponding energy error bar at this wavelength is about ±24meV.

Supplementary Table 1. List of experimental conditions under laser and xenon illuminations, respectively.

Light source	Beam size (mm^2)	P (μW)	Percentage on device	Actual power $\tilde{P}$(μW)	Intensity (W/cm^2)
Laser	0.096	45	100%	45	$4.7x10^{-2}$
Xenon lamp	0.375	30	25%	7.5	$2x10^{-3}$

Supplementary Table 2. List of all fitting parameters (C1,C2,L1,L2 and D) of **Fig. S1(D,E)** using equ. (1) in main text.

λ(nm)	C1	C2	L1	L2	C1/L2	D
535nm, laser	0.26±0.01	-0.02±0.01	0.06±0.01	0.36±0.01	0.72	24.8±0.05
532nm, xenon	0.13±0.01	-0.01±0.01	-0.01±0.01	0.16±0.01	0.85	3.1±0.05

As can be seen, C1 and L2 are about one order of magnitude larger than C2 and L1, respectively. Under laser illumination, D is about 8 times larger and the actual power 6 time larger as those obtained using the xenon lamp. This is probably due to larger photothermal effect from smaller laser beam [2]. Furthermore, C1(L2) with laser illumination is roughly 2x as much as with xenon. Nevertheless, the ratio between CPGE (C1) and LPGE (L2) does not change too much (within 20 %) in these two cases. These test results show that extra care must be taken to make sure any comparisons are conducted under same experimental conditions.

SM3. λ/4 waveplate (QWP) effect on the CPGE results

There was a recent report on possible artifacts from the rotation of λ/4 waveplate (QWP). A summary of this report is as follows: (1) intensity variation through the QWP; (2) photothermal current modulated by the QWP [2]. While the former is mainly due to nonuniformity of the waveplate and has period of 2π, the latter can bring in both sine and cosine terms of 2α and 4α, possibly complicating the real CPGE and LPGE terms. These artifacts cause particularly serious problems in the work of ref. [2] because the material used was a semimetal, and the QWP was at mid-infrared (CdSe) which has larger nonuniformity over the QWP area than the quartz waveplate we have used. We have conducted thorough investigations on our system and concluded that these artifacts are negligible, and do not cause alternation of the real experimental data. Details of our investigation are presented:

(1) Influence of the light intensity variation after the λ/4 waveplate on the C, L, and D parameters

We measured the power of excitation light vs the rotation angle of the λ/4 waveplate at three different wavelengths, 480 nm (IB), 530 nm ($EX_{\sigma+}$) and 535 nm, as shown in **Supplementary Figure 2 (A).** The power of the excitation light was measured in the same setup for CW PGE current measurement by replacing the device with a depolarizer and a silicon detector. To show that the variation of the excitation light power has little effect in the PGE(α) spectra, we divided the PGE current with the normalized power of the excitation light. The original C1/D at 480 nm, 530 nm and 535 nm were 1.80 %, 1.72 % and 1.05 %, respectively. Whereas the corrected C1/D at 480 nm, 530 nm and 535 nm were 1.73 %, 1.68 % and 1.08 %, respectively. **Supplementary Figure 2 (B-D)** show the change on PGE (α) spectra after the correction, and **Supplementary Table 3** lists details of λ/4 waveplate effect on other parameters. As can be seen, the intensity variation from the λ/4 waveplate affects C1 about 2 % to 4%, and L2 4 % to 7%. Therefore, we conclude that the variation of the λ/4 wave-plate transmission has little effect on the PGE(α) spectra. The larger fluctuation in C2 and L1 are due to the much smaller magnitude of these coefficients. In any case C2 and L1 are not important for the discussion since the CPGE and LPGE are dominated by C1 and L2, respectively.

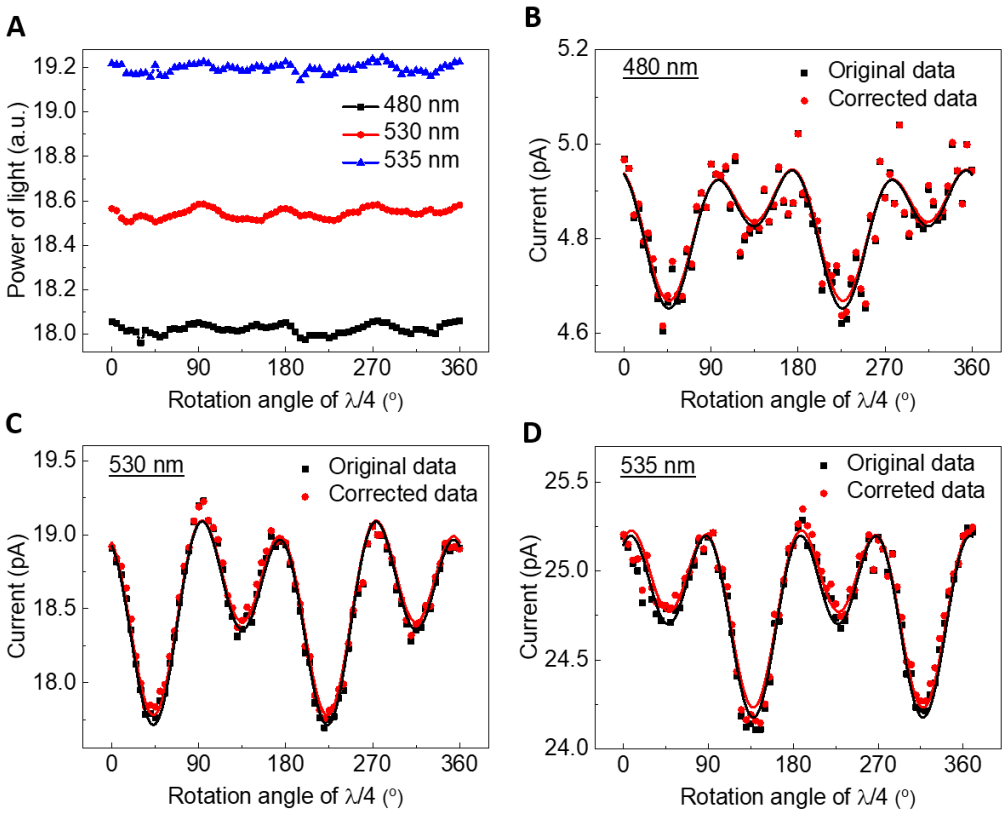

Supplementary Figure 2. (A) The power of the excitation light vs. the rotation angle α of the λ/4 waveplate at three different wavelengths, 480 nm (black), 530 nm (red) and 535 nm (blue). (B)-(D) The original PGE (α) current (black dot) and the corrected PGE (α) current (red dot) normalized by the excitation power at excitation 480 nm (**B**), 530 nm (**C**) and 535 nm (**D**). The black and red lines in the panels are fittings using the equ (1) in the main text. All the data are measured at the same conditions as those in **Fig. 2B** in the main text.

Supplementary Table 3. List of the λ/4 waveplate effect on the fitting parameters (C1,C2,L1,L2).

λ (nm)	**ΔC1/C1 (%)**	ΔC2/C2 (%)	ΔL1/L1 (%)	**ΔL2/L2 (%)**
535	**3.0**	40	5.5	**6.9**
530	**1.9**	1.0	1.0	**4.5**
480	**3.8**	60	60	**6.1**

(2) Misalignment (α_0) between the λ/4 waveplate fast axis and light excitation polarization direction

This unintentional and inevitable experimental error, α_0 was estimated to be less than a few degrees, mostly 1 degree to 5 degree. This does not place much difference in the C's and L's values.

(3) Photothermal current /Seebeck effect

According to ref. [2], photothermal current has both sin(2α) and cos(2α) (for the CPGE terms) and sin(4α) and cos(4α) (for the LPGE terms). However, this effect is minimal in our samples because:

1) Low free carrier density ($n \approx 10^{13}$ cm^{-3}) and low carrier mobility (μ=(0.1 to 1) $cm^2/V{\cdot}s$, comparing with the reference semimetal sample ($n \approx (10^{18}$ to $10^{19})$ cm^{-3}; μ=(10^4 to 10^5) $cm^2/V{\cdot}s$).

2) Very thick sample with average thickness of (8 to 10) μm, more than 20x the penetration depth, therefore the difference in absorption coefficient along the fast and slow axis of λ/4 waveplate does not matter *since all photons are absorbed in any case*.
3) The only possible non-zero term that might have small contribution to the PGE current is the cos(2α) term, estimated to be about 0.3 % of the DC background current. Our C1 (for sin(2α) is between 1 % to 5 % of the total DC background current (D). Since C2 (for cos(2α)) is 1 order of magnitude smaller than C1, it is possible that photothermal current makes some contribution in the cos(2α) term.
4) Very low power of xenon lamp (<30 μW) and large beam size (cover the whole device area) further minimize the Seebeck effect.

In conclusion, we believe that the PGE current that we measured is basically free from known artifacts.

SM4. Photoconductivity action spectrum

In this measurement, the incandescent light from a Xe lamp, which was dispersed through a monochromator, was used to excite the same device used in the CPGE measurement. We also measured the conductivity by sweeping the voltage applied to the device with a Keithley 238 multimeter [3]. The voltage was swept in a symmetrical way (0 V to -5 V, +5V to -5 V, -5V to 0 V). The photoconductivity was then subtracted by linearly fitting the I-V curve from +5 V to -5 V. This procedure was adopted from ref. [4].

SM5. Action spectra of the CPGE (C1), LPGE (L2) and DC offset (D)

Supplementary Figure 3 (**A-C**) shows the action spectra of circular photogalvanic effect (CPGE), linear photogalvanic effect (LPGE) and the DC offset (D) at resonant excitation of exciton with various azimuthal angles ϕ'. Please note that there is an angle ψ between the azimuthal angle in measurement (ϕ') and that in the theoretical calculation (ϕ) (see the experiment setup in **Fig. 1C**). As can be seen in **Supplementary Figure 3**, both CPGE and LPGE depend on ϕ', and there are polarity change of the photocurrent for both LPGE and CPGE. However, there's minimal dependence of D on ϕ', due to the slight intensity variation at different ϕ' angle. **Supplementary Figure 3 (D)** also shows that CPGE (C1) is not the first derivative of absorption(d(OD)/dE), for both exciton and interband excitations. **Supplementary Figure 4 (A)** compares the D internal quantum efficiency (IQE) spectrum with that of the photoconductivity (PC) IQE spectrum, both are normalized. D-IQE spectrum is very similar to the PC-IQE spectrum measured at -5V bias, inferring that there is a weak electric field within the device although the applied voltage is zero. We speculate this weak field comes from the photothermal effect (proportional to absorption) and photovoltaic effect (from slight asymmetry among the two electrodes) [2,4]. The two IQE spectra have nearly identical onset at both exciton and IB transitions, where the absorption has minima. Based on the comparison between PC current @ (-5V) and the DC offset current D, we estimate the internal electric field E_{PGE} is about 2 orders of magnitude smaller than the electric field E_{PC}=5(V)/10μm (in the device used for PC measurement). Since the two crystals have similar thickness (~10μm), $E_{PGE}=10^{-2}E_{PC}=10^{-2}(5(V)/10\mu m)) = 5x10^4$ V/m=$5x10^2$V/cm, which is 3 orders of magnitude smaller than a typical electric field in electroabsorption measurement [5]. As another comparison, we took a look at the electric field inside a typical solar cell made with similar RP 2D perovskite [6]. At the exciton energy (2.5eV), the external quantum efficiency is about 5%. The built-in electric field in their device is estimated as:

$$E_{built-in} = \frac{\Delta V_{buit-in}}{d} = \frac{0.5V}{200nm} = 2.5 \times 10^4\, {}^{V}/_{cm} >> 500\, {}^{V}/_{cm} \;\; in\ our\ PGE\ device$$

Therefore we expect the internal electric field at zero bias in our device used for PGE measurements is too weak to dissociate the excitons.

It is interesting to see that the IQE for exciton and IB carriers are almost the same in the PC action spectrum; however, more than doubled in D action spectrum. Due to the much stronger electric field (> 2 orders) in PC measurement, both exciton dissociation and free carriers (electrons and holes) separation may be equally efficient. Based on the coincidence of CPGE peak with the lower energy exciton (EX1) at 2.3 eV, we conjecture that the exciton might dissociate via the edge states, or other native defect sites [6].

Supplementary Figure 4(B) shows a comparison between the PC-IQE and absorption spectra at room temperature and low temperature (10K). It is seen that the redshift of PC with respect to absorption is much less at T=10K, when the localized/trap states at the absorption edge become unavailable (or frozen).

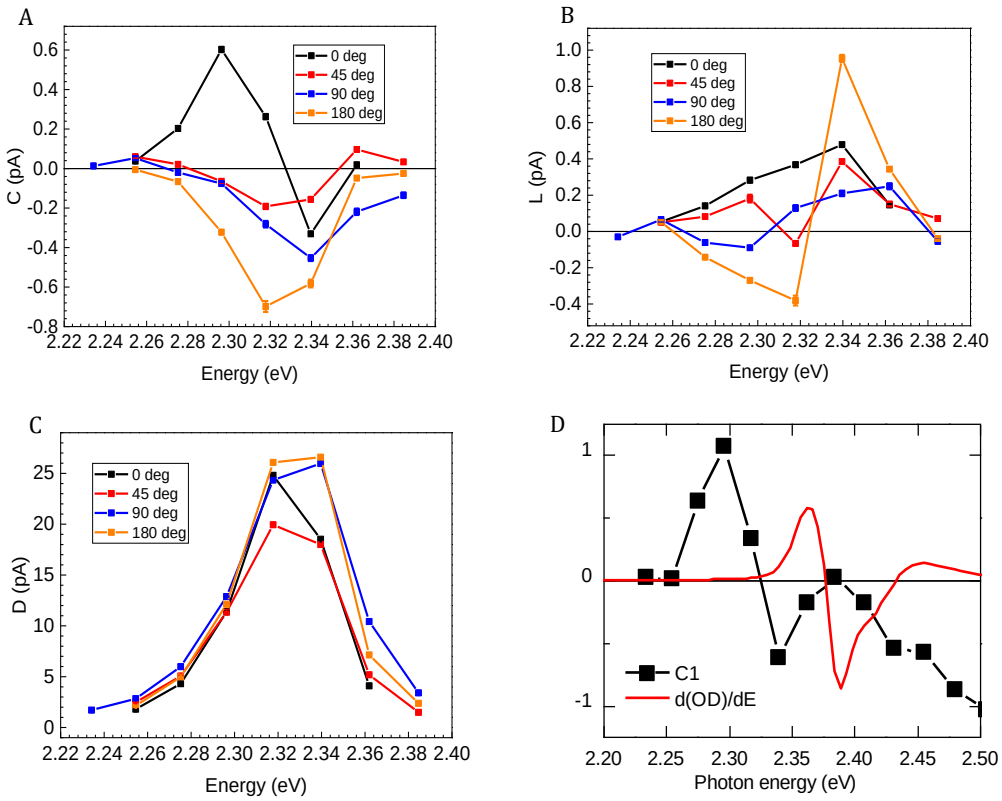

Supplementary Figure 3. Action spectrum of (**A**) C1, (**B**) L2, (**C**) D at resonant excitation with the exciton band at $\theta=30^0$ with various ϕ' angles, as shown in each figure. (**D**) shows the comparison between (C1) at $\phi=0^0$ (black symbol) with the first derivative of the absorption spectrum (red line). We conclude from this comparison that C1 spectrum is not due to the derivative of the absorption spectrum.

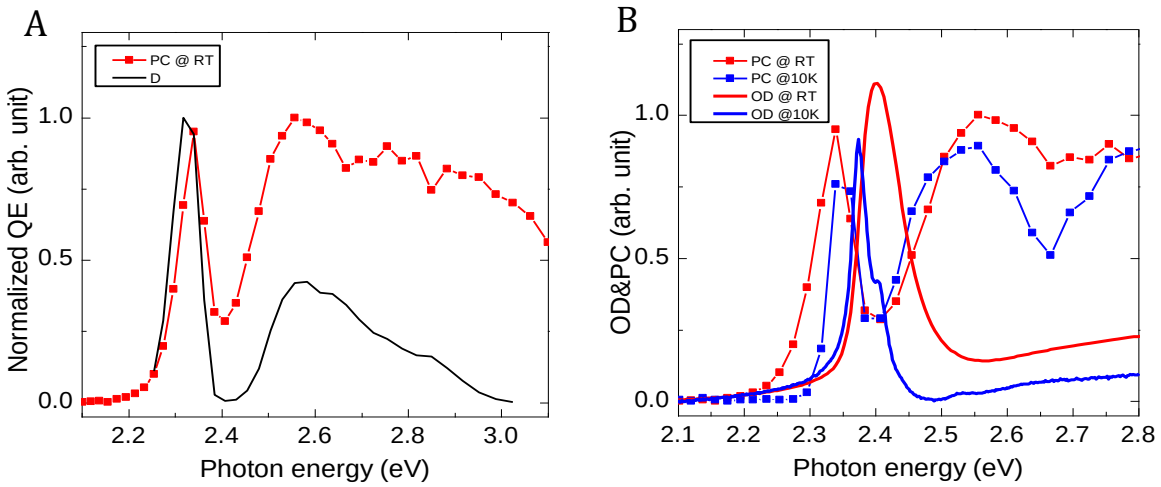

Supplementary Figure 4. (**A**) Normalized internal quantum efficiency (QE) action spectrum of photoconductivity (PC) (symbol) and DC offset D (line); PC measurement was taken with a reverse bias of 5 volt; (**B**) Comparison of the absorption at room temperature (RT, red line) and T=10 K (blue line); PC-IQE at room temperature (RT, red symbol) and T=10 K (blue symbol). At low temperature, the absorption red-shifts while PC-IQE blue-shifts.

SM6. SEM and XRD characterizations of the 2D-PEPI crystals

The 2D-PEPI crystals were characterized using a scanning electron microscope (SEM), FEI Helios Quanta, at low vacuum of 4.8 mTorr (≈0.064 Pa), to avoid charging effects on sample and substrate. Images were taken at different magnification showing uniform growth of ≈ 3 mm size crystals, where higher magnification images at the edge of the crystal show layered structure highlighting the 2D layered structure of the crystals. **Supplementary Figure 5** shows SEM images at 57X and 500 X. The film thickness was characterized using a profilometer, Tencor P 10. The thickness was measured along across the length of crystals showing a fairly smooth morphology with a nominal crystal thickness was found to be 8 µm to13 µm thick, consistent with that in ref [1].

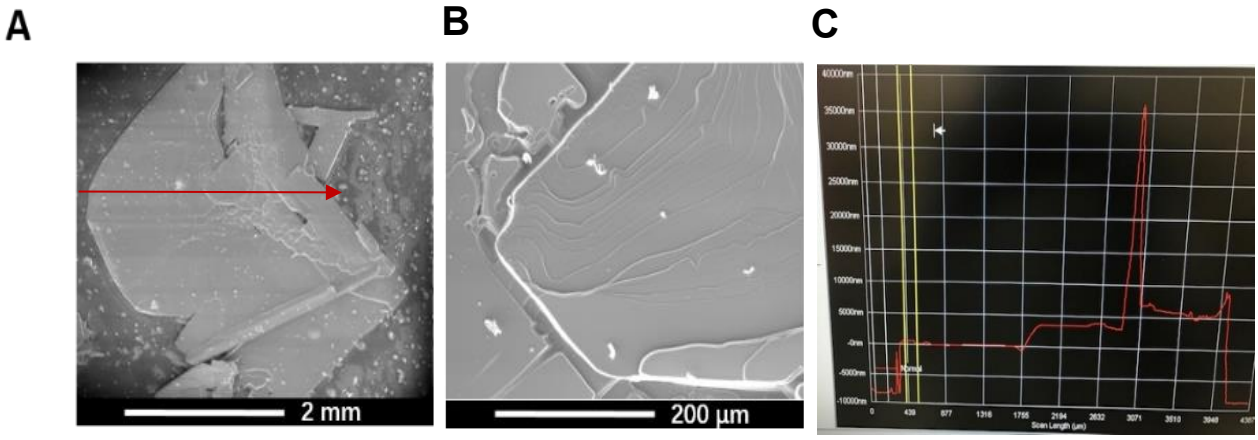

Supplementary Figure 5. Scanning electron micrograph (SEM) images of 2D-PEPI crystals. **(A)**. The crystal shown is about 2 mm x 4mm. **(B)**. Zoom-in image shows the layered structure, with the stacking direction normal to

the quartz substrate. **(C)**. The height profile measured along the redline in A. The spike was from an anomaly also shown as a white dot in A.

Finally (out-of-plane) x-ray diffraction pattern was measured using Bruker D2 Phaser. The 2-theta scan shows highly crystalline growth along the c-axis, as shown in **Supplementary Figure 6**. The calculated inter-layer distance is c = 3.25 nm, consistent with earlier reports [7, 8]. SEM images combined with XRD spectrum points to relatively large single crystal [1].

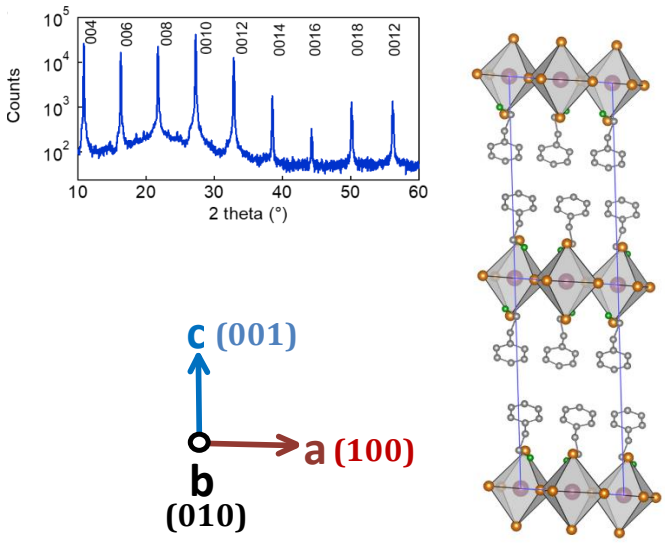

Supplementary Figure 6. X-ray diffraction pattern (XRD) of 2D-PEPI crystal grown on quartz substrate (upper left panel). The X-ray source is Cu-K_α line (λ=0.154 nm). The right panel shows the side view of the crystal structure with $[PbI_6]^{4-}$ layers parallel to the quartz substrate.

SM7. AFM measurement of the 2D-PEPI single crystal

The 2D-PEPI single crystal morphology and roughness were measured using BrukerDimesion Icon atomic force microscope (AFM) utilizing the scan-assist tapping mode. A region of 25 μm x 25 μm was scanned with lateral resolution of 12.2 nm and height resolution of ≈2 nm using AFM tip having 2 nm nominal diameter. The data was analyzed using Bruker Nano scope Analysis software where prior to image processing, a linear flattening was applied to account of tilts and low frequency noise. The average roughness was computed using RMS over the complete scan.

Supplementary Figure 7 shows the topography of two crystals that we measured. Crystal 1 shows a terrace like structure over multiple layers corresponding to 2D nature of the PEPI crystals. The larger roughness was a result of scanning across multiple layers (4 layers), so the average roughness is about 3.34 nm to 4.675 nm. The scanning region of Crystal 2 was on single layer which shows its smooth surface with roughness of 3.82 nm. The observed step height is also consistent with the c = 3.25 nm estimated from XRD (see **Supplementary Figure 6** and discussion).

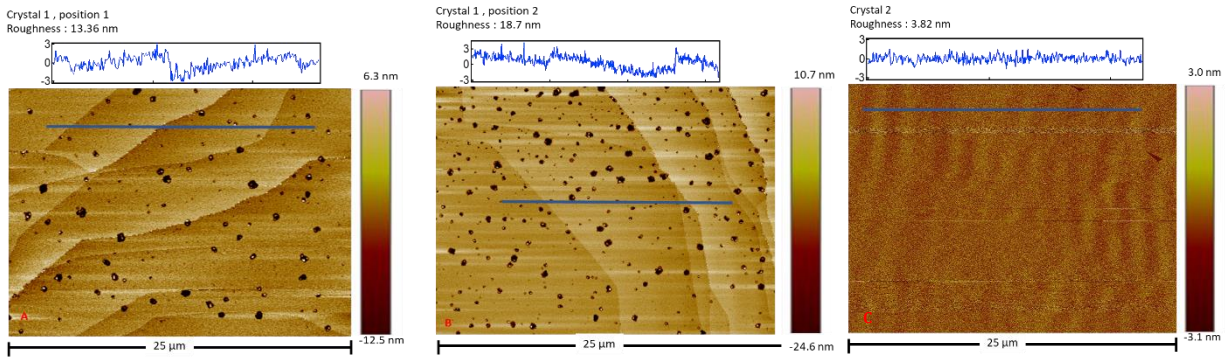

Supplementary Figure 7. AFM topography of two different 2D-PEPI crystals. The dark spots shown in A&B are tiny pin holes (smaller than sub-micrometer).

SM8. Other optical characterizations

All optical measurements were done at room temperature in air. The absorption (or optical density) was measured using a UV/Vis spectrometer (Olis). For the photoluminescence (PL) measurement, a 2D-PEPI single crystal was excited using a 30 mW CW laser at 486 nm. We used two different setup configurations, respectively to measure the PL emission spectrum from the flat side of the crystal (surface-PL) and PL emission from the edge of the crystal (edge-PL) (see **Supplementary Figure 8, inset**). In both cases, the PL spectrum was recorded by an Ocean Optics USB4000 spectrometer via an optical fiber. The two different PL spectra are shown in **Supplementary Figure 8**. Both spectra show a dominant contribution from excitons. The edge PL band is red-shifted with respect to the surface-PL band by about 60 meV, similar to previous reports in other 2D lead perovskites crystals [6,9]. The edge effect indicates the existence of layer edge defect states which were shown to facilitate excitons dissociation into long-lived free carriers [6].

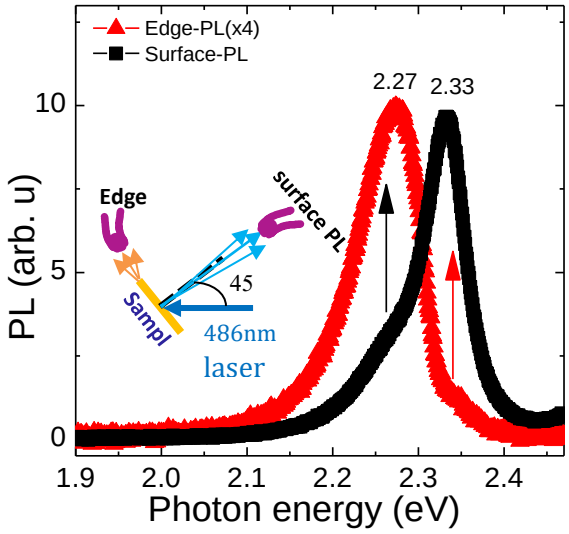

Supplementary Figure 8. Room temperature photoluminescence (PL) spectra of 2D-PEPI crystal collected from the front (surface-PL, black symbol) and the edge of the crystal (edge-PL, red symbol). The excitation was a CW 486 nm diode laser with power of 30 mW, and the spectra were recorded by a commercial Ocean Optics USB4000 spectrometer.

The surface-PL band peaks at 2.33eV namely EX2 in **Fig. 1B**, with low energy shoulder at the same position as the edge-PL peak (2.27eV). On the other hand, the edge-PL spectrum contains a small high

energy shoulder that coincides with the surface-PL band. The mutual inclusion of these two PL band in the two measurement geometries indicates the co-existence of free exciton and edge state exciton in our 2D-PEPI crystal.

SM9. Terahertz emission measurements

***Set-up*.** Terahertz emission from 2D-PEPI crystals was measured by an electro-optic sampling technique using standard time-domain spectroscopy configuration. The samples were excited by 0.25 μJ pulses at 405 nm generated using type-I BBO crystal pumped with 810 nm pulses from Ti-Sapphire regen-amplified laser system at 1 KHz repletion rate. 2D-PEPI crystals on Quartz substrate were excited from the quartz side. The emitted terahertz radiation due to photo-excited carriers was collected by 2 parabolic mirrors and focused on to 0.5 mm thick electro-optic ZnTe <110> crystal. The terahertz field pulse signal was measured as the change in polarization of the probe beam induced as a result of electro-optic sampling technique, as measured by a Wollaston prism and a set of balanced silicon detectors using lock-in technique. We note that the measured bandwidth of the emitted signal detection technique is limited by the detection crystal. To measure the polarization dependent terahertz field, the sample was mounted on a rotation stage and the excitation beam was modulated using λ/2 and λ/4 plate. In addition, a wiregrid polarizer was placed in the collimated beam path between the two parabolic mirrors, to allow detection of polarization emitted terahertz field. A schematic diagram of the experimental setup is shown in **Supplementary Figure 9**.

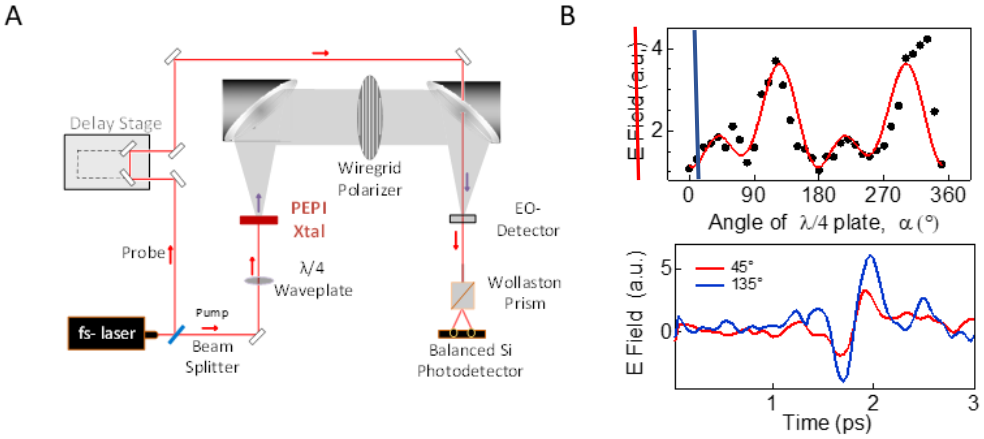

Supplementary Figure 9. (**A**). Schematic representing the time domain terahertz emission setup. (**B**). upper panel: THz emission field due to ultrafast photogalvanic current in 2D-PEPI crystals measured along x' direction, as a function of the rotation angle, α, between the excitation pump polarization and the fast axis of a λ/4 waveplate; lower panel: time domain THz signals at the marked α angles ($\alpha=45^0$ for RCP, and $\alpha=135^0$ for LCP. The excitation is from 3.06 eV of the fs pulse laser at θ=45°.

Simultaneous Terahertz emission measurements for $E_{x'}$ and $E_{y'}$:

Since terahertz measurements are non-contact measurements it allows us to measure ultrafast currents along the two orientations simultaneously. Here the wiregrid polarizer, the probe beam and detection electro-optic crystals were rotated by 90° to measure the field emission along the orthogonal polarization. The THz field emission $E_{x(y)}$ is related to ultrafast photocurrent $J_{x(y)}(t) \sim e^{-\frac{t}{\tau}}$ in a simple form:

$$E_{x(y)} \propto \frac{dJ_{x(y)}(t)}{dt} \propto \left|J_{x(y)}(t)\right| \quad (1)$$

Therefore we expect the same formulae for $J_{x(y)}$ would apply to $E_{x(y)}$. For the dependence on rotation angle α of the λ/4 plate, we can use a similar form as equ. (1) in the main text to fit the experimental data, other than a proportional coefficient with the unit of $[A \cdot m/S]$.

$$E_{x(y)} \propto L1_{x(y)} \sin(4\alpha) + L2_{x(y)} \cos(2\alpha) + C1_{x(y)} \sin(2\alpha) + C2_{x(y)} cos\ (2\alpha)\ + D \quad (2)$$

Furthermore, as shown in **Fig.1C**, there is an angle ψ between the measurement x' and the crystal a-axis (x-axis in **Fig. 1C**). So, we have the following equations for the measured $E_{x'(y')}$:

$$E_{x'} = E_x cos\ \psi + E_y\ sin\ \psi \quad (3)$$

$$E_{y'} = E_x \sin\psi + E_y\ cos\ \psi \quad (4)$$

We focus on the two dominant parameters, namely, *C1* for CPGE, and *L2* for LPGE. Details on derivation of *C1* and *L2* can be found in **Auxiliary Supplementary Materials**.

Based on Supplementary equ. (2)-(4), for $E_{x'}$, we get:

$$C1_{x'} = C1_x cos\ \psi + C1_y\ sin\ \psi \quad (5)$$

$$L2_{x'} = L2_x cos\ \psi + L2_y\ sin\ \psi \quad (6)$$

For $E_{y'}$, we have

$$C1_{y'} = C1_x sin\ \psi + C1_y\ cos\ \psi \quad (7)$$

$$L2_{y'} = L2_x sin\ \psi + L2_y\ cos\ \psi \quad (8)$$

With:

$$C1_x = sin\theta\ sin\ \phi\gamma_{xy} - cos\ \theta\gamma_{xz}\ (S9)$$

$$C1_y = -sin\ \theta cos\ \phi\gamma_{yx}\ \ (S10)$$

$$L2_x = -\frac{1}{4} sin\ (2\theta)\ cos\phi\chi_{xxz} + \frac{1}{8}(3 + cos\ (2\theta)\ )sin\ (2\phi)\ \chi_{xxy}\ \ (S11)$$

$$L2_y = -\frac{1}{4}\sin 2\theta \sin\phi\ \chi_{yyz} + \frac{1}{4}\left[\chi_{yxx}\left(\cos^2\theta\cos^2\phi - \sin^2\phi\right) + \chi_{yyy}\left(\cos^2\theta\sin^2\phi - \cos^2\phi\right)\right]\ (S12)$$

In this experiment, we use s-polarized excitation polarized along y' direction, so the plane of incidence is along x' direction therefore $\phi' = 0^0$, accordingly, $\phi = \phi' - \psi = 0 - \psi = -\psi$ (see **Fig. 1A**). For the case of normal incidence ($\theta = 0^0$), Supplementary equ (9)-(12) can be simplified as:

$$C1_x = -\gamma_{xz}\cos\psi\ \ (9')$$

$$C1_y = 0\ \ (10')$$

$$L2_x = -\frac{1}{2}\sin(2\psi)\ \ (11')$$

$$L2_y = \frac{1}{4}\left(\chi_{yxx} - \chi_{yyy}\right)\cos(2\psi)\ \ (12')$$

Supplementary equ.(5) –(8) then give:

$$C1_{x'} = -\gamma_{xz}\cos^2\psi \quad (5')$$

$$C1_{y'} = -\gamma_{xz}\sin\psi\cos\psi \quad (6')$$

$$L2_{x'} = -\frac{1}{2}\sin(2\psi)\cos\psi + \frac{1}{4}(\chi_{yxx} - \chi_{yyy})\cos(2\psi)\sin\psi \quad (7')$$

$$L2_{y'} = -\frac{1}{2}\sin(2\psi)\sin\psi + \frac{1}{4}(\chi_{yxx} - \chi_{yyy})\cos(2\psi)\cos\psi \quad (8')$$

From Supplementary equ. (5') and (6'), we can get a simple expression to determine the angle ψ as:

$$\psi = \tan^{-1}(\frac{C1_{y'}}{C1_{x'}}) \quad (13)$$

Supplementary Figure 10 shows the field emission profiles of two orientations (x'and y'). The red line is fitting using equ. (S2). **Supplementary Table 4** lists all fitting parameters. $\psi = (24\pm21)^0$ in this measurement. The big uncertainty is due to the not-so-satisfying fitting for $E_{y'}$ (goodness of fitting or adjusted-R^2 is only 0.74). As can be seen in **Supplementary Figure 11**, the error bars are generally bigger for *C1* than for *L2*, probably due to the small value of *C1* at normal incidence.

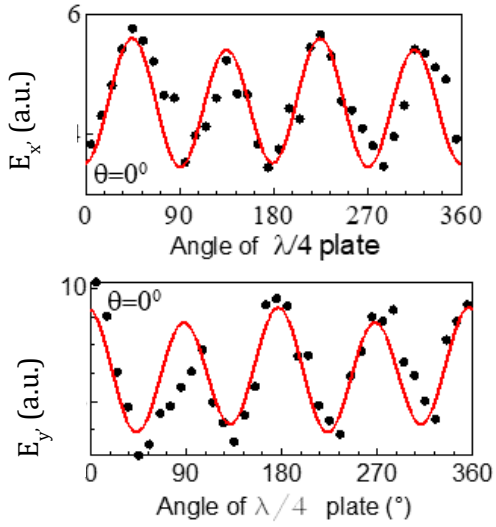

Supplementary Figure 10. Polarized terahertz emission due to ultrafast photogalvanic currents in 2D-PEPI crystals. $E_{x'}$ and $E_{y'}$ represent terahertz field emission along x' and y' direction respectively, as a variation of excitation pump polarization modulated by rotation of a λ/4 waveplate. The fields $E_{x'}$ and $E_{y'}$ were subsequently measured using probe beam and wire grid polarizer along the respective direction. The excitation is from 3.06 eV of the fs pulse laser at ϑ=0°.

Supplementary Table. 4. The best fitting parameters for **Supplementary Figure 9** using Supplementary equ. (2).

Field direction	**C1**	C2	L1	**L2**	D
$E_{x'}$	**0.207±0.089**	-0.0881±0.149	0.0111±0.148	**-0.796±0.149**	4.58±0.106
$E_{y'}$	**-0.0928±0.124**	-0.195±0.131	-0.187±0.187	**0.981±0.199**	8.53±0.140

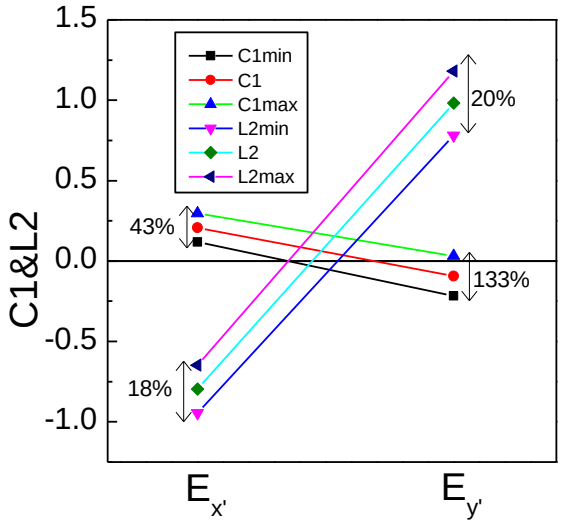

Supplementary Figure 11. Details of *C1* and *L2* in **Table S4**. with error range marked by the arrow (error bar, s.e.m.).

The analysis shows that we can use the simultaneous measurements of $E_{x'}$ and $E_{y'}$ to determine the unknown **angle** ψ for each crystal sample. It also can be seen that C1 in both directions are very close to zero, this indicates that the degree of in-plane inversion symmetry is much smaller within the plane (along y-direction or *b*-axis) than out-of-plane (along *z*-direction).

Terahertz emission of optical phonons

In order to distinguish the THz emission from optical phonons from that resulted from the ultrafast current in CPGE in 2D-PEPI as shown in **Supplementary Figure 9**&**10**, we measured the optical phonon modes using terahertz transmission through the crystal with respect to the reference substrate. **Supplementary Figure 12** below shows the THz emission from CPGE current (**Supplementary Figure 12 (A)**) and its Fourier transform spectrum (**Supplementary Figure 12 (B**)). For comparison, **Supplementary Figure 12 (C)** shows the measured absorption spectrum in the THz range through the PEPI crystal that shows the optical phonon modes at 0.78 THz and 1.6 THz, respectively. These phonons are probably associated with Pb-I-Pb rocking vibration and Pb-I stretching bonds as observed before [10]. It is worth pointing out that, while the THz emission from the ultrafast CPGE current is primarily at ~1THz (see **Supplementary Figure 9 (B) and Fig. 3B**), the frequency ranges at 0.8 THz and above 1.6 THz are suppressed. This is due to the fact that we measured terahertz emission in transmission mode through the crystal, where photo-absorption and emission happen from limited thickness of the crystal. The transmission of the emitted radiation though the thickness of 7-10 μm of the crystal would cause subsequent absorption of the signal to a significant amount at resonance with those phonon frequencies. Therefore, the measured THz radiation is peaked at 1 THz where the dip between the two phonons is observed. We thus conclude that the presence of emitted signal in **Supplementary Figure 9 (B) and Fig. 3B** at complementary frequencies to those of the phonons (**Supplementary Figure 12 (C)**).

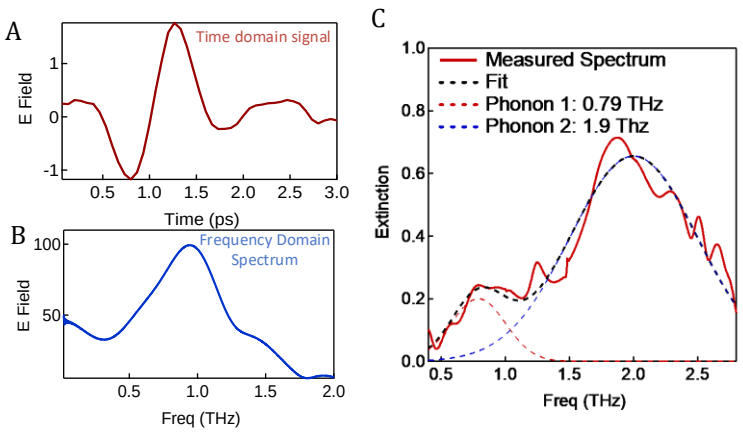

Supplementary Figure 12: (**A**). The transient THz emission and its Fourier transform spectrum (**B**) measured from PEPI crystal, compared to the crystal absorption spectrum measured in the THz range (**C**). The spectrum is decomposed into two phonon modes as indicated.

***<u>Terahertz emission measurements upon varying the half wave plate (λ/2) angle</u>*:**

We have also measured terahertz emission from 2D-PEPI upon varying the angle of λ/2 wave-plate, as shown in **Supplementary Figure 13,** left panel. The origin of the linear photogalvanic effect (LPGE) that results in terahertz emission could be attributed to two possible processes: *(i)* 'Optical rectification' as second-order non-linear process; and (ii) 'shift current' resulting from the displacement of the wave function center upon transitioning from valence to conduction band (as shown schematically in **Supplementary Figure 13**, right panel). Both mechanisms require non-centrosymmetric crystal symmetry which could arise of off-center positioning of lead ion, Pb^{2+}, in the in-plane PbI_6^{4-} octahedrons. Previous studies have identified a strong coupling between phonon modes and photoexcited states in 2D-PEPI, and other ferroelectric oxides such as $KTaO_3$ [11] exhibit a dynamic Jahn-Teller effect upon photoexcitation. The possibility of photoinduced changes in symmetry is reserved for future studies.

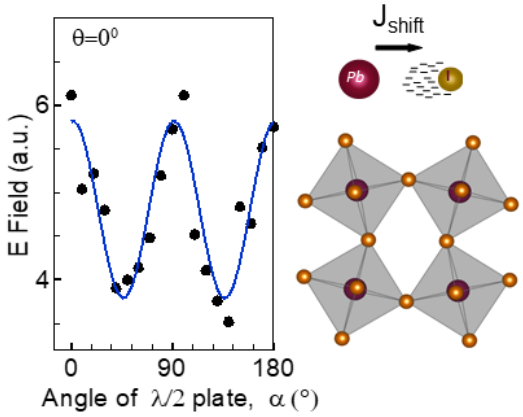

Supplementary Figure 13. Terahertz emission intensity as a function of the rotation angle of a λ/2 waveplate. The fitting is done using ~cos(4α) term. The schematic shown in the right panel represents photoinduced shift of charge to more electronegative I^- in Pb-I bond. This hypothesis relies on off-center Pb^{2+} in PbI_6^{-4} octahedron, as possible origin of non-zero shift current in 2D-PEPI crystal.

Excitation power variation as function of quarter waveplate (λ/4) angle:

To calibrate the uniformity of average power of 400 nm incident excitation pulses, we measured the average power using a polarization insensitive thermal power meter as a function of quarter wave plate angle. We calculated corresponding photon density, *N*, of excitation pulses using the relation $= \alpha \frac{\varepsilon_p}{E_{ph} A}$, where α is absorption coefficient, ε_p is the pulse energy, E_{ph} is the energy per photon at 400 nm and A is the excitation beam area. Given the defined parameters remains same, the photon density with rotation angle of λ/4 waveplate was found to be fairly constant, with random fluctuation less than 2 % (see **Supplementary Figure 14**). Therefore this small variation could be regarded as arbitrary and disregarded as the factor causing the observed trends of CPGE and LPGE.

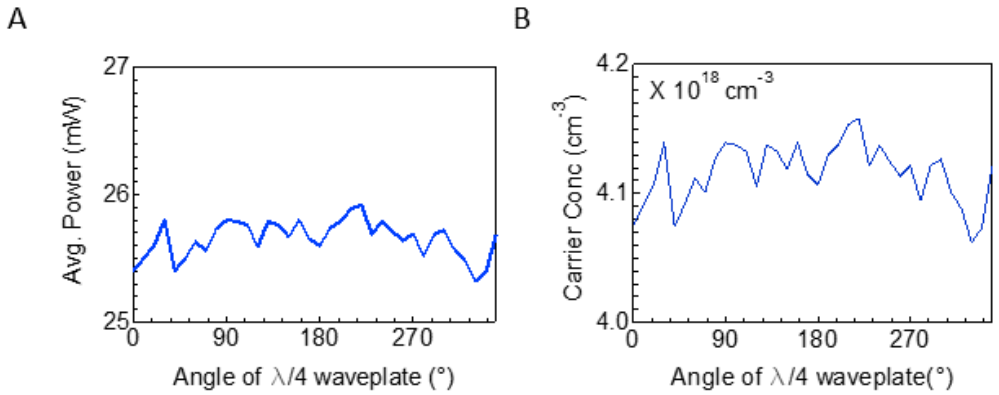

Supplementary Figure 14. (**A**) The power of excitation pulsed light vs. the rotation angle of the quarter-wave plate at 405 nm. **(B)** corresponding calculated carrier density as variation of angle of quarter wave plate. Overall 2 % change in carrier density was observed while no particular trend is present. This is estimated to have a minimal impact on trends observed in terahertz emission from 2D PEPI crystal.

SM10. Transient circularly polarized photoinduced absorption measurements

The transient polarization modulated photoinduced circular reflection/absorption (so called circular-PPA) apparatus is schematically shown in **Supplementary Figure 15**. It is a derivative of the well-known optical pump/probe spectroscopy. In regular pump/probe (or photoinduced absorption PIA) spectroscopy, the pump pulses that are modulated by an optical chopper or acoustic optic modulator (AOM) are absorbed by the sample and generate photoexcitations (excitons or electron and hole pairs); whereas the probe pulse is used to monitor the population in various states of these photoexcitations. Both pump and probe beams are aligned through various optical components in order to spatially and temporally overlap them on the sample. In this case the photoexcitations dynamics is measured by temporally delaying the probe pulses with respect to the pump pulses using a mechanically delayed stage.

Unlike the regular pump/probe spectroscopy, in our circular-PPA setup, only the polarization of the pump beam is modulated using a PhotoElastic Modulator (PEM) at 41 kHz, between left and right circular polarization. The probe beam is also circularly polarized for circular-PPA. In the present study, the pump and probe beams were split from the output of a Ti: Sapphire laser (Spectra-Physics) with pulse duration of 150 fs and 80 MHz repetition rate that can be turned from 730 nm to 810 nm. In addition, the pump beam was optically doubled to ~ 400 nm by a second harmonic generation crystal, whereas the probe beam was at ~ 530 nm from a combination of the idler beam with the fundamental at 800 nm. In order to

minimize the large scattering from the strong pump beam into the detector, we used a double modulation scheme in which in which the probe beam was also modulated by a mechanical chopper at 1.2 kHz. The pump beam with average intensity of 3 Wcm^{-2} and much weaker probe beam were focused onto a small area of the sample (either single crystal or thin film) having a spot size of ~100 µm in diameter. The probe beam reflected (or transmitted) intensity was measured with a silicon photodetector connected to the first lock-in amplifier that was externally synchronized with the chopper frequency. The second lock-in amplifier was externally synchronized with the PEM modulation frequency. This experimental set-up has a superior sensitivity for measuring the spin relaxation time than the transient Faraday rotation or regular polarized pump/probe technique.

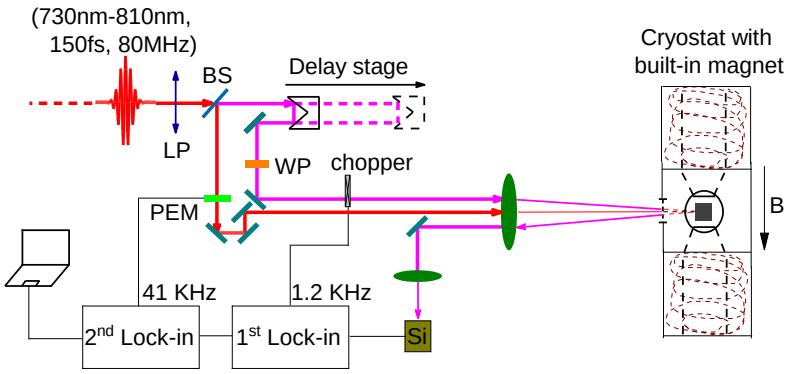

Supplementary Figure 15: Experimental apparatus for polarization modulated photoinduced circular reflection/absorption technique. PEM stands for a photoelastic modulator that changes the pump beam polarization between left and right circular polarization. WP is a quarter wavelength plate for the circular-PPR (or PPA); LP is a linear polarizer, and BS is a beam-splitter. Double lock-in technique was used to minimize the pump scattering into the photodetector.

Firstly, we measured a 'circular polarization memory' at the exciton level at room temperature using the transient polarized photoinduced absorption technique at 537 nm with 150 fs time resolution. In this method we set the pump beam polarization at a fix circular polarization, whereas the circular polarization of the probe beam was modulated between same circular polarization or opposite polarization to that of the pump beam. In this method only the difference between the same or opposite pump-probe circular polarizations is measured. Indeed, we found that there is 'circular polarization memory' for the exciton, in which the photoinduced absorption is larger when the pump-probe have same polarization than that of pump-probe with opposite polarization (see **Supplementary Figure 16**). This shows that the excitons are spin polarized upon absorption by a circular polarized pump and maintain the polarization even at room temperature.

Secondly, we measured the lifetime of this circular polarization memory. **Supplementary Figure 17** shows the transient circular PPA response of a 2D-PEPI crystal at room temperature. As can be seen, the spin relaxation process has two time constants (TC); a fast TC of 2.3 ps and a slower TC of 14.6 ps. The fast TC may be related to the exciton thermalization, whereas the slower TC is for the decay of thermalized excitons. The average spin relaxation time is about 4.5ps, meaning that the exciton and the resulting electron-hole pairs that follow exciton dissociation in 2D-PEPI lose their spin alignment within 4.5 ps, which is much longer than the momentum relaxation time in this material (~ 100 fs). This explains the lack of THz emission (ultrafast within tens of femtoseconds) from the photocurrent upon exciton

excitation with circularly polarized light. We therefore consider spin-galvanic effect (SGE) to be the mechanism for the photocurrent at exciton transition. Details are given in the main text.

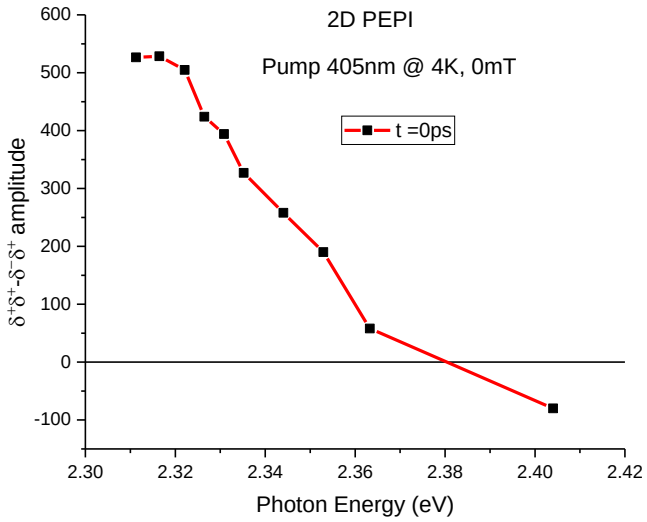

Supplementary Figure 16. Transient polarization modulated photoinduced circular absorption spectrum measured at time t=0 at 4K and zero magnetic field at 405 nm excitation. The signal at room temperature was too small for measuring the spectrum in this configuration. However, we were able to get the spin dynamics as shown in **Supplementary Figure 17**.

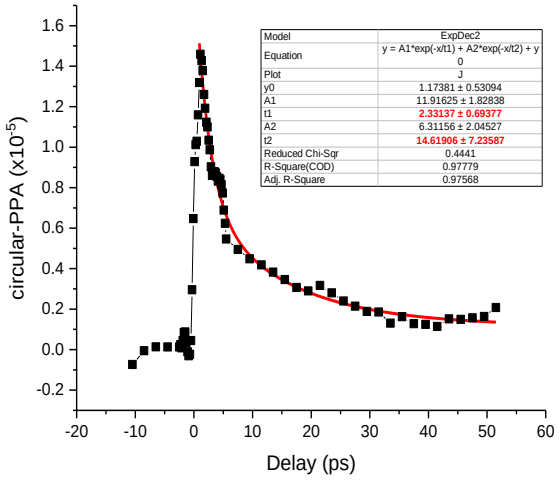

Supplementary Figure 17. Transient circularly polarized pump-probe absorption (PPA) of a 2D-PEPI crystal measured at room temperature using pump at 410 nm and probe at 537 nm, in resonance with the exciton transition. The line through the data points is a fit using a double exponential function with time constants of 2.3 ps and 14 ps, respectively, from which we obtain an average spin relaxation time of ~ 4.5 ps.

SM11. Theoretical calculation of symmetry tensors

Summary of the calculation: For the third order tensor, χ_{ijk} (symmetric among the 2nd and 3rd indices) related to the LPGE the first index indicates the current flow direction, and the 2nd and 3rd indexes stand for the optical field. For instance, χ_{xzx} corresponds to current flowing in the x-direction as a result of absorption of light of the form $\vec{E}(\hat{z}+\hat{x})$. Our model is capable of reproducing the experimental features, as seen in the satisfactory fitting shown in **Fig. 2C.** Here we show, by employing a more elaborate fitting procedure to fit the same experimental data, that we can extract more details on the crystal symmetry.

In the PGE (θ) measurement, the light source before the λ/4 plate is *p*-polarized, equivalent to $\beta=0^0$ in the general formula presented in the **Auxiliary Supplementary Materials**. The azimuthal angle ϕ in the theoretical calculation is related to the azimuthal angle ϕ' in experiment by: $\phi = \phi' - \psi$ (see **Fig. 1C** for the definitions of angles). The data in **Fig. 2C** were taken with $\phi'=90^0$, therefore $\phi = 90^0 - \psi$. The θ dependence of LPGE (*L2*) and CPGE (*C1*) are derived to be:

$$L2(\theta) = \tfrac{1}{4}sin\psi\{\cos(\psi)[(3+\cos(2\theta))\cos(\psi)\chi_{xxy} - \sin(2\theta)\,\chi_{xxz}] + (-\cos^2\psi + \cos^2\theta\sin^2\psi)\chi_{yxx} + (-\sin^2\psi + \cos^2\theta\cos^2\psi)\chi_{yyy} - sin(2\theta)\,cos\psi\chi_{yyz}\} \quad (14)$$

$$C1(\theta) = \sin(\theta)\left[\cos^2\psi\,\gamma_{xy} - \sin^2\psi\,\gamma_{yx}\right] - \cos(\theta)\cos(\psi)\,\gamma_{xz} \quad (15)$$

Please note that Supplementary equ. (14) and (15) can be simplified (by omitting details of symmetry tensors) as:

$$L2(\theta) = A'\sin 2\theta + B'\cos 2\theta + G \quad (14')$$

$$C1(\theta) = A\sin\theta + B\cos\theta \quad (15')$$

These are the equations used in the fitting shown in **Fig. 2C&D** in the main text, with various coefficients being:

$$A' = -\frac{1}{8}\sin(2\psi)\left(\chi_{xxz} + \chi_{yyz}\right)$$

$$B' = \frac{1}{8}\sin\psi\left[\cos^2\psi\left(2\chi_{xxy} + \chi_{yyy}\right) + (\sin^2\psi)\chi_{yxx}\right]$$

$$G = \frac{1}{8}\sin\psi\left[\chi_{yyy}(\cos(2\psi) - \sin^2\psi) - \chi_{yxx}(\cos(2\psi) + \cos^2\psi) + 6\cos^2\psi\chi_{xxy}\right]$$

$$A = \cos^2\psi\,\gamma_{xy} - \sin^2\psi\,\gamma_{yx}$$

$$B = -\cos(\psi)\,\gamma_{xz}$$

The fitting parameters used in **Supplementary Figure 18** are 8 non-zero components of χ & γ tensors including: 2 non-zero components of χ tensor (χ_{xxz} and χ_{yyz}), and 2 non-zero components of γ tensor (γ_{xy} *and* γ_{yx}) for out-of-plane inversion asymmetry along z-axis; 3 non-zero components of χ tensor (χ_{xxy}, χ_{yxx} and χ_{yyy}), and 1 non-zero components of γ tensor (γ_{xz}) for in-plane inversion asymmetry along y-axis, as well as angle ψ between the current direction and the crystal a-axis as defined in **Fig. 1C**. Among all 9 parameters, the ones that matter are listed in **Supplementary Table 5**. The best fitting of *L2(θ)* (blue line in **Supplementary Figure 18)** shows that there are two non-zero elements χ_{yyy} and χ_{yxx}, confirming that the crystal symmetry is C_i with in-plane inversion symmetry breaking along the crystal *b*-

axis. The fitting of *C1(θ)* (orange line in **Supplementary Figure 18**) shows that, for the second-rank pseudo tensor γ_{ij}, the dominant term is γ_{yx}, indicating out-of-plane inversion symmetry breaking along z-direction. The fitting also yields near zero γ_{xz}, indicating negligible in-plane inversion symmetry breaking, which seems to contradict the result from the L2(θ) fitting. However, this apparent contradiction is incorrect. The fitting also yields ψ=87^0, meaning that the current direction chosen in our measurement is almost along the crystal *b*-axis (in-plane inversion symmetry breaking direction). In theory, the CPGE current is null when it is measured along the symmetry breaking axis [12]. Therefore it is expected that γ_{xz} is near zero. The appearance of in-plane symmetry breaking is subtler in the *C1* curve, but can be seen in the fact that the magnitude of *C1* looks systematically larger for $\theta > 0$ than it is for $\theta < 0$.

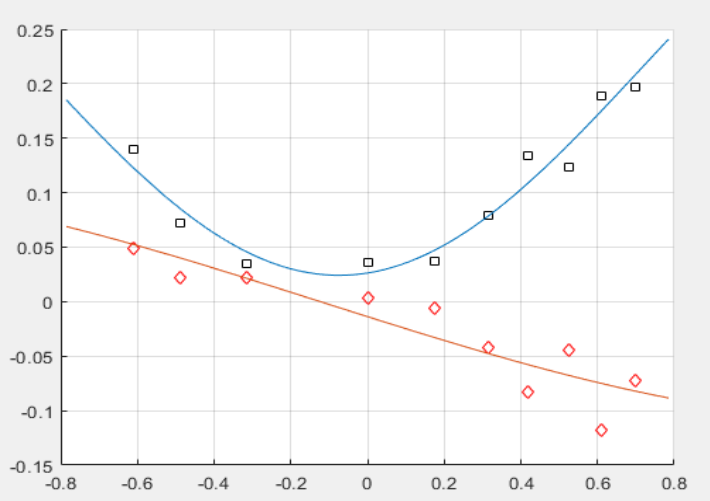

Supplementary Figure 18. Fitting of the extracted LPGE, *L2(θ)* (blue line) and CPGE, *C1(θ)* (orange line) parameters using Supplementary equ. (14) and equ. (15), respectively. The x-axis has the unit of radian. The open symbols are the experimental data that are also presented in **Fig. 2C**.

Supplementary Table 5. lists the five important parameters extracted using Supplementary equ. (14) and (15). The other four parameters do not affect the fitting results in noticeable way, and their values are not important.

χ tensor	χ_{yyy}	χ_{yxx}	γ tensor	γ_{yx}	γ_{xz}		ψ (rad/degree)
	-1.6	-1.5		0.11	<<0.1		1.52(87)

SM12. Two band calculation of the CPGE action spectrum

The orbital character of the conduction and valence band in 2D-PEPI is similar to that of 3D $MAPbI_3$. In particular, the conduction band is primarily spin-orbital split Pb p-orbital with total angular momentum $J = 1/2$, whereas the valence band is composed of Pb s-orbitals and I p-orbitals, with overall s=1/2 characteristic. The basis functions for the conduction and valence band electrons are therefore given by:

$$\left|J_{+1/2}\right\rangle = \frac{1}{\sqrt{3}}(|(X+iY)\downarrow\rangle + |Z\uparrow\rangle)$$

$$\left|J_{-1/2}\right\rangle = \frac{1}{\sqrt{3}}(|(X-iY)\uparrow\rangle - |Z\downarrow\rangle)$$

$$|S_{+1/2}\rangle = |S\uparrow\rangle$$

$$|S_{-1/2}\rangle = |S\downarrow\rangle$$

where X, Y, Z denote real-valued $L = 1$ spherical harmonic function p_x, p_y, p_z, respectively. As discussed in the main text, the experimental data indicates that the out-of-plane symmetry breaking is more substantial than the in-plane symmetry breaking. Accordingly, we consider a minimal $k \cdot p$ model with an out-of-plane symmetry-breaking Rashba term (along the z-direction). In the basis of $|J_{+1/2}\rangle$, $|J_{-1/2}\rangle$, $|S_{+1/2}\rangle$, $|S_{-1/2}\rangle$, the Hamiltonian is given by:

$$H = \begin{pmatrix} (k_x^2 + k_y^2)t_p + \epsilon_0 & (ik_x + k_y)\alpha_c & 0 & -(ik_x + k_y)\xi \\ (k_y - ik_x)\alpha_c & (k_x^2 + k_y^2)t_p + \epsilon_0 & -(ik_x - k_y)\xi & 0 \\ 0 & -(-ik_x - k_y)\xi & (-k_x^2 - k_y^2)t_s & (ik_x + k_y)\alpha_v \\ -(k_y - ik_x)\xi & 0 & (k_y - ik_x)\alpha_v & (-k_x^2 - k_y^2)t_s \end{pmatrix},$$

where $t_{p(s)}$ is the intra-orbital hopping between $p(s)$ bands, $\alpha_{c(v)}$ is the Rashba coefficient for conduction(valence) bands respectively, and ξ is the interband hybridization which enables electron-hole couplings. Note that k is taken to be dimensionless (scaled by inverse lattice constant a^{-1}), and $\alpha_{c(v)}$ is given in units of energy.

The general expression for the circular photogalvanic effect at zero temperature is given as [13]:

$$\gamma_{ij} = \tau \frac{2\pi e^3}{\hbar^2} \int d\boldsymbol{k}\, \epsilon_{j\ell m} \sum_{cv} \left|M_{cv}^{\ell m}(\boldsymbol{k})\right|^2 \delta(E_c(\boldsymbol{k}) - E_v(\boldsymbol{k}) - \hbar\omega) \left(\frac{dE_c}{dk_i} - \frac{dE_v}{dk_i}\right),$$

where τ is the momentum relaxation time, $\epsilon_{j\ell m}$ is the antisymmetric tensor, $M_{cv}^{\ell m} = \langle\psi_c|(\hat{r}^\ell + i\hat{r}^m|\psi_v\rangle$. $\hat{r}^\ell$ is the dipole operator, which for extended dimensions is related to the velocity operator: $\langle\psi_c|\hat{r}^\ell|\psi_v\rangle = i\left\langle\psi_c\left|\frac{dH}{dk_\ell}\right|\psi_v\right\rangle/(E_c - E_v)$. For the 2D model, we cannot define a velocity matrix with z component. However, the conduction bands include a Z-orbital component which leads to nonzero dipole matrix in z direction,

$$r_z = \begin{pmatrix} 0 & 0 & -z & 0 \\ 0 & 0 & 0 & z \\ -z^* & 0 & 0 & 0 \\ 0 & z^* & 0 & 0 \end{pmatrix},$$

where z parameterizes the oscillator strength.

Expanding in the small parameter ξ/ϵ_0, we obtain the following closed form expression for the photogalvanic tensor for current along the x-direction upon absorption of incident light circularly polarized along the y-direction:

$$\gamma_{xy} = \frac{2\xi \mathrm{Re}(z)}{(\hbar\omega)^2 t} \times \begin{cases} 2\sqrt{t(E_R + \hbar\omega - \epsilon_0)}(4E_R + \hbar\omega - 2\epsilon_0) & \text{for } \epsilon_0 - E_R \le \hbar\omega \le \epsilon_0 \\ \alpha(4E_R + 3\hbar\omega - 4\epsilon_0) & \text{for } \hbar\omega > \epsilon_0 \end{cases}$$

where $t = t_s + t_p$, $\alpha = \alpha_c + \alpha_v$. This response exhibits a peak at $\hbar\omega = E_R = (\alpha_c + \alpha_v)^2/4(t_s + t_p)$. Note that this expression is valid for any *sign combination* of Rashba splitting for valence and conduction band. This expression can be formulated in terms of effective mass model of band edges by identifying $t_{c,v} = \hbar^2/(2a^2 m^*_{c,v})$, where a is the lattice constant. Then $E_R = E_d - (m^*_c + m^*_v)(\alpha_c + \alpha_v)^2/(2\hbar^2)$.

The addition of broadening substantially smears out the tail of the response (the analytical expressions are cumbersome and not presented here). The numerical expression for γ_{ij} including a broadening energy η is:

$$\gamma_{ij} = \tau \frac{2e^3}{\hbar^2} \int d\boldsymbol{k}\, \epsilon_{j\ell m} \sum_{cv} \left| M^{\ell m}_{cv}(\boldsymbol{k}) \right|^2 \frac{\eta}{\eta^2 + (E_c(\boldsymbol{k}) - E_v(\boldsymbol{k}) - \hbar\omega)^2} \left(\frac{dE_c}{dk_i} - \frac{dE_v}{dk_i} \right).$$

The large impact of smearing can be understood as a consequence of the large density of states at the conduction/valence band edges. The shift of the band extrema away from $k = 0$ leads to a density of states that diverges as $E^{-1/2}$ as the energy approaches the band edge. Significant spectral weight is therefore available to be shifted from above the band edge to below. Numerically, we find that a qualitatively similar spectrum is obtained over a range of Rashba energies E_R and smearing energies (or broadening) η when both are in the range of 10's of meV. The choice of broadening parameter is consistent with other references [14]. This provides a limit on the precision with which the model determines the value of Rashba splitting. The fitting result is shown in part in **Fig. 2B**, with **Supplementary Figure 19 (A)** shows the range of parameters for E_R and η in unit of meV. manuscript.

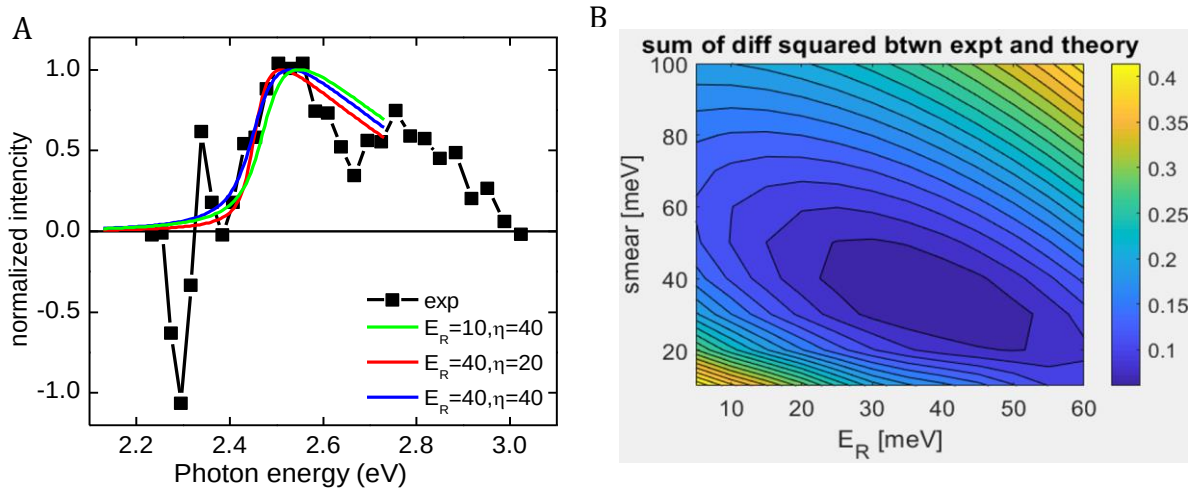

Supplementary Figure 19. (**A**). Comparison of experimental CPGE action spectrum (also shown in **Fig. 2B** in the main text) with calculation using different Rashba energies (E_R) and broadening parameters (η). (**B**). Sum of difference squared between computed and measured CPGE values, as a function of Rashba energy E_R and broadening parameter η. The experimental values used for comparison are limited to the energy range 2.38 eV to 2.55 eV.

More accurate estimate may be achieved when fitting with low temperature data which is under way. **Supplementary Figure 19 (B)** shows a comparison of the model fit to experimental data as a function of Rashba splitting energy E_R and broadening parameter η. We compute the sum of the squares of the difference between the (normalized) measured and computed values of the CPGE intensity. Based on this

result we obtain Rashba splitting (E_R) of 35±10 meV and broadening parameter (η) of 30±10 meV as given in the

Supplementary References

1. Lédée, F. *et al*. Fast growth of monocrystalline thin films of 2D layered hybrid perovskite. *CrystEngComm* **19**, 2598-2602 (2017).
2. Osterhoudt, G. B. *et al.* Colossal mid-infrared bulk photovoltaic effect in a type-I Weyl semimetal. *Nature Materials* **18**, 471–475 (2019).
3. The full description of the procedures used in this paper requires the identification of certain commercial products. The inclusion of such information should in no way be construed as indicating that such products are endorsed by NIST or are recommended by NIST or that they are necessarily the best software for the purposes described.
4. Niesner, D. *et al.* Structural fluctuations cause spin-split bands in $(CH_3NH_3)PbI_3$: Experimental evidence from circular photogalvanic effect. *PNAS*, **115**, no. 38, 9509–9514(2018).
5. Zhai, Y. *et al.*, Giant Rashba splitting in 2D organic-inorganic halide perovskites measured by transient spectroscopies, *Sci. Adv.* **3**: e1700704 (2017).
6. Blancon, J.-C. *et al*. Extremely efficient internal exciton dissociation through edge states in layered 2D perovskites. *Science* **355**, 1288–1292 (2017).
7. Fieramosca, A. *et al.* Out-of-Plane Excitons in 2D Single-Crystal Perovskites. *ACS Photonics* **5**, 4179−4185(2018).
8. Calabrese, J. *et al.* Preparation and Characterization of Layered Lead Halide Compounds. *J. Am. Chem. Soc*. **113**, (2328-2330)1991.
9. Mao, L. et al., Hybrid Dion−Jacobson 2D Lead Iodide Perovskites, J. Am. Chem. Soc. 2018, 140, 3775−3783.
10. M. Sender *et al.*, Optical phonons in methylammonium lead halide perovskites and implications for charge transport, Materials Horizons 3, 613-620 (2016).
11. Vikhnin, V.S., Eglitis, R.I., Kapphan, S.E., Borstel, G., Kotomin, E.A., Polaronic-type excitons in ferroelectric oxides: Microscopic calculations and experimental manifestation. *PHYSICAL REVIEW B*, **65**, 104304 (2002).
12. Ganichev,S.D. *et al.*, Removal of spin degeneracy in p-SiGe quantum wells demonstrated by spin photocurrents, PHYSICAL REVIEW B **66**, 075328 (2002).
13. Aversa, C., J. E. Sipe, J.E., Nonlinear optical susceptibilities of semiconductors: Results with a length-gauge analysis. *Phys. Rev. B* **52** 14636 (1995).
14. Neutzner, S. *et al.* Exciton-polaron spectral structures in two-dimensional hybrid lead-halide perovskites. *PHYSICAL REVIEW MATERIALS* **2**, 064605 (2018).

We start with general form for linearly polarized light, followed by the interaction with the quarter wave plate. The resulting incident optical field is input into the symmetry-allowed form of the conductivity tensor to find the in-plane components of the DC electric current. The dependence of this current on the quarter wave plate angle α is expressed in terms of the sum d+c1 sin(2α)+l1 sin(4α) + l2 cos(4α). All steps are included in order to illustrate the logic/math behind the procedure.

```
(* general (θ,ϕ) of incident light angle.  Assume surface normal is in the z-
 hat {0,0,1} direction *)
s = {-Sin[ϕ], Cos[ϕ], 0};
p = {-Cos[θ] Cos[ϕ], -Cos[θ] Sin[ϕ], Sin[θ]};
(* suppose the incoming polarization
  vector (n1) is rotated by angle β with respect to the p-
 polarization vector.  β=0⁰(90⁰) is for p-polarized(s-polarized)*)

n1 = Cos[β] p + Sin[β] s;
n2 = -Sin[β] p + Cos[β] s;
```

```
(* QWP mixes n1 and n2 according to angle α between (n1) and fast-
 axis of QWP crystal *)
(* r is rotation matrix to connect (n1,n2) basis to fast-
 slow axis basis (i.e. diagonal basis) of the QWP *)
r[α_] := {{Cos[α], Sin[α]}, {-Sin[α], Cos[α]}};
(* transmission in the diagonal basis of QWP: transmission for fast wave=1,
transmission for slow wave=i *)
t = {{1, 0}, {0, I}};
(* the transfer function of QWP in (n1,n2) basis is defined below *)
qwp = Inverse[r[α]].t.r[α];
(* get transmitted field in n1,
n2 basis (assuming incoming light is polarized along n1) *)
transmitted = FullSimplify[qwp.{1, 0}];
(* now get transmitted wave in {x,y,z}-basis *)
e = FullSimplify[transmitted[[1]] n1 + transmitted[[2]] n2];
(* manual complex conjuate *)
ec = {(-1/2 - I/2) ((-I Cos[β] + Cos[2 α + β]) Cos[θ] Cos[ϕ] +
        (-I Sin[β] + Sin[2 α + β]) Sin[ϕ]), (1/2 - I/2)
     (Cos[ϕ] (Sin[β] + I Sin[2 α + β]) - I (-I Cos[β] + Cos[2 α + β]) Cos[θ] Sin[ϕ]),
    (1/2 - I/2) (Cos[β] + I Cos[2 α + β]) Sin[θ]};
```

The following section considers out-of-plane symmetry breaking only

```
(* response tensors for out-of-
 plane symmetry breaking.  Since z is inequivalent to -z,
tensor components with an odd number of z indices are nonzero *)
χt_xxz = χ_xxz {{0, 0, 1}, {0, 0, 0}, {1, 0, 0}};
χt_yyz = χ_yyz {{0, 0, 0}, {0, 0, 1}, {0, 1, 0}};
γt_xy = I γ_xy {{0, 0, 1}, {0, 0, 0}, {-1, 0, 0}};
γt_yx = I γ_yx {{0, 0, 0}, {0, 0, 1}, {0, -1, 0}};

(* answer for jx *) jx = FullSimplify[ec. (χt_xxz + γt_xy) .e]
(* answer for jy *) jy = FullSimplify[ec. (χt_yyz + γt_yx) .e]
```

$$\text{Sin}[\theta]\ \Big(\text{Sin}[2\,\alpha]\ \text{Sin}[\phi]\ \gamma_{xy} - \Big(\big(\text{Cos}[\beta]^2 + \text{Cos}[2\,\alpha+\beta]^2\big)\ \text{Cos}[\theta]\ \text{Cos}[\phi] + \text{Cos}[2\,\alpha]\ \text{Sin}[2\,(\alpha+\beta)]\ \text{Sin}[\phi]\Big)\ \chi_{xxz}\Big)$$

$$\text{Sin}[\theta]\ \Big(-\text{Cos}[\phi]\ \text{Sin}[2\,\alpha]\ \gamma_{yx} + \text{Cos}[2\,\alpha]\ \text{Cos}[\phi]\ \text{Sin}[2\,(\alpha+\beta)]\ \chi_{yyz} - \frac{1}{2}\ (2 + \text{Cos}[2\,\beta] + \text{Cos}[2\,(2\,\alpha+\beta)])\ \text{Cos}[\theta]\ \text{Sin}[\phi]\ \chi_{yyz}\Big)$$

```
(* rewrite current expression jx in terms of Sin[2α], Sin[4α], Cos[4α] *)
d = -1/2 Sin[θ] (Cos[θ] Cos[ϕ] (2 + Cos[2 β]) + Sin[2 β] Sin[ϕ]) χ_xxz;
c1 = Sin[θ] Sin[ϕ] γ_xy;
l1 = 1/2 Sin[θ] (Cos[θ] Cos[ϕ] Sin[2 β] - Cos[2 β] Sin[ϕ]) χ_xxz;
l2 = -1/2 Sin[θ] (Cos[2 β] Cos[θ] Cos[ϕ] + Sin[2 β] Sin[ϕ]) χ_xxz;
jxform2 = d + c1 Sin[2 α] + l1 Sin[4 α] + l2 Cos[4 α];

(* rewrite current expression jy in terms of Sin[2α], Sin[4α], Cos[4α] *)
d = 1/2 Sin[θ] ( Sin [2 β] Cos[ϕ] - 2 Cos[θ] Sin[ϕ] - Cos[2 β] Cos[θ] Sin[ϕ]) χ_yyz;
c1 = -Sin[θ] Cos[ϕ] γ_yx;
l1 = 1/2 Sin[θ] (Cos[2 β] Cos[ϕ] + Sin[2 β] Cos[θ] Sin[ϕ]) χ_yyz;
l2 = 1/2 Sin[θ] ( Sin[2 β] Cos[ϕ] - Cos[2 β] Cos[θ] Sin[ϕ]) χ_yyz;
jyform2 = d + c1 Sin[2 α] + l1 Sin[4 α] + l2 Cos[4 α];
```

Experiments have control over (θ,ϕ,β), and can measure (D,c1,l1,l2). We use these expressions to determine the nonzero (χ,γ) components, which in turn tells us the symmetry.

The following section considers in-plane symmetry breaking only

```
(* response tensors for in-plane symmetry breaking,
take symm-breaking to be in y-direction.  Now we can have
  nonzero tensor components with an odd number of y indices *)
χtxxy = χxxy {{0, 1, 0}, {1, 0, 0}, {0, 0, 0}};
χtyxx = χyxx {{1, 0, 0}, {0, 0, 0}, {0, 0, 0}};
χtyyy = χyyy {{0, 0, 0}, {0, 1, 0}, {0, 0, 0}};
γtxz = I γxz {{0, 1, 0}, {-1, 0, 0}, {0, 0, 0}};

(* general answer for jx *)
jxInPlaneSymmBreak = FullSimplify[ec. (χtxxy + γtxz) .e]
```

$$-\text{Cos}[\theta]\ \text{Sin}[2\,\alpha]\ \gamma_{xz} + \frac{1}{4}\left(-2\ \text{Sin}[\theta]^2\ \text{Sin}[2\,\phi] + \text{Cos}[2\,\alpha]\right.$$
$$\left.(-4\ \text{Cos}[\theta]\ \text{Cos}[2\,\phi]\ \text{Sin}[2\,(\alpha+\beta)] + \text{Cos}[2\,(\alpha+\beta)]\ (3+\text{Cos}[2\,\theta])\ \text{Sin}[2\,\phi])\right)\ \chi_{xxy}$$

```
(* general answer for jy *)
jyInPlaneSymmBreak = FullSimplify[ec. (χtyxx + χtyyy) .e]
```

$$\frac{1}{2}\left(\left(\left(\text{Sin}[\beta]^2 + \text{Sin}[2\,\alpha+\beta]^2\right)\ \text{Sin}[\phi]^2 + \text{Cos}[\theta]\right.\right.$$
$$\left.\left(\left(\text{Cos}[\beta]^2 + \text{Cos}[2\,\alpha+\beta]^2\right)\ \text{Cos}[\theta]\ \text{Cos}[\phi]^2 + \text{Cos}[2\,\alpha]\ \text{Sin}[2\,(\alpha+\beta)]\ \text{Sin}[2\,\phi]\right)\right)$$
$$\chi_{yxx} + \left(\text{Cos}[\phi]^2\left(\text{Sin}[\beta]^2 + \text{Sin}[2\,\alpha+\beta]^2\right) + \text{Cos}[\theta]\left(\left(\text{Cos}[\beta]^2 + \text{Cos}[2\,\alpha+\beta]^2\right)\right.\right.$$
$$\left.\left.\text{Cos}[\theta]\ \text{Sin}[\phi]^2 - \text{Cos}[2\,\alpha]\ \text{Sin}[2\,(\alpha+\beta)]\ \text{Sin}[2\,\phi]\right)\right)\ \chi_{yyy}\Big)$$

```
(* rewrite current expression jx in terms of Sin[2α], Sin[4α], Cos[4α] *)
```

$$\text{d} = 1/4\left(-2\ \text{Sin}[\theta]^2\ \text{Sin}[2\,\phi] - \right.$$
$$\left.2\ \text{Cos}[\theta]\ \text{Cos}[2\,\phi]\ \text{Sin}[2\,\beta] + \frac{1}{2}\ \text{Cos}[2\,\beta]\ (3+\text{Cos}[2\,\theta])\ \text{Sin}[2\,\phi]\right)\ \chi_{xxy};$$
$$\text{c1} = -\text{Cos}[\theta]\ \gamma_{xz};$$
$$\text{l1} = 1/4\left(-2\ \text{Cos}[2\,\beta]\ \text{Cos}[\theta]\ \text{Cos}[2\,\phi] - \frac{1}{2}\ (3+\text{Cos}[2\,\theta])\ \text{Sin}[2\,\beta]\ \text{Sin}[2\,\phi]\right)\ \chi_{xxy};$$
$$\text{l2} = 1/4\left(-2\ \text{Cos}[\theta]\ \text{Cos}[2\,\phi]\ \text{Sin}[2\,\beta] + \frac{1}{2}\ \text{Cos}[2\,\beta]\ (3+\text{Cos}[2\,\theta])\ \text{Sin}[2\,\phi]\right)\ \chi_{xxy};$$
$$\text{jxInPlaneSymmBreakform2} = \text{d} + \text{c1}\ \text{Sin}[2\,\alpha] + \text{l1}\ \text{Sin}[4\,\alpha] + \text{l2}\ \text{Cos}[4\,\alpha];$$

```
(* rewrite current expression jy in terms of Sin[2α], Sin[4α], Cos[4α] *)
d = 1 / 2 χyxx 1/2 (Cos[β]^2 (3 Cos[θ]^2 Cos[ϕ]^2 + Sin[ϕ]^2) +
      Sin[β]^2 (Cos[θ]^2 Cos[ϕ]^2 + 3 Sin[ϕ]^2) + Cos[θ] Sin[2 β] Sin[2 ϕ]) +
    1 / 2 χyyy (1/2 (Sin[β]^2 (3 Cos[ϕ]^2 + Cos[θ]^2 Sin[ϕ]^2) +
        Cos[β]^2 (Cos[ϕ]^2 + 3 Cos[θ]^2 Sin[ϕ]^2) - Cos[θ] Sin[2 β] Sin[2 ϕ]));
c1 = 0;
l1 = 1 / 2 χyxx
     (1/2 (-Cos[θ]^2 Cos[ϕ]^2 Sin[2 β] + Sin[2 β] Sin[ϕ]^2 + Cos[2 β] Cos[θ] Sin[2 ϕ])) +
    1 / 2 χyyy (1/2 (Sin[2 β] (Cos[ϕ]^2 - Cos[θ]^2 Sin[ϕ]^2) - Cos[2 β] Cos[θ] Sin[2 ϕ]));
l2 = 1 / 2 χyxx (1/2 (Cos[2 β] (Cos[θ]^2 Cos[ϕ]^2 - Sin[ϕ]^2) + Cos[θ] Sin[2 β] Sin[2 ϕ])) +
    1 / 2 χyyy (1/2 (Cos[2 β] (-Cos[ϕ]^2 + Cos[θ]^2 Sin[ϕ]^2) - Cos[θ] Sin[2 β] Sin[2 ϕ]));
jyInPlaneSymmBreakform2 = d + c1 Sin[2 α] + l1 Sin[4 α] + l2 Cos[4 α];
```

Here we summarize the results of coefficients d, c1, l1,l2 in the case of in-plane inversion symmetry breaking along y-axis (or crystal b-axis) and out-of-plane inversion symmetry breaking along z-axis.

$$(* \text{ out-of-plane symmetry breaking } *)$$

$$(*\text{for jx } *)$$

$$\text{dxop}[\theta\_, \phi\_, \beta\_] := -\frac{1}{2} \text{Sin}[\theta] \, (\text{Cos}[\theta] \, \text{Cos}[\phi] \, (2 + \text{Cos}[2\,\beta]) + \text{Sin}[2\,\beta] \, \text{Sin}[\phi]) \, \chi_{xxz};$$

$$\text{c1xop}[\theta\_, \phi\_, \beta\_] := \text{Sin}[\theta] \, \text{Sin}[\phi] \, \gamma_{xy};$$

$$\text{l1xop}[\theta\_, \phi\_, \beta\_] := \frac{1}{2} \text{Sin}[\theta] \, (\text{Cos}[\theta] \, \text{Cos}[\phi] \, \text{Sin}[2\,\beta] - \text{Cos}[2\,\beta] \, \text{Sin}[\phi]) \, \chi_{xxz};$$

$$\text{l2xop}[\theta\_, \phi\_, \beta\_] := -\frac{1}{2} \text{Sin}[\theta] \, (\text{Cos}[2\,\beta] \, \text{Cos}[\theta] \, \text{Cos}[\phi] + \text{Sin}[2\,\beta] \, \text{Sin}[\phi]) \, \chi_{xxz};$$

$$(* \text{ for jy } *)$$

$$\text{dyop}[\theta\_, \phi\_, \beta\_] :=$$

$$\frac{1}{2} \text{Sin}[\theta] \, (\text{Sin}\,[2\,\beta] \, \text{Cos}[\phi] - 2 \, \text{Cos}[\theta] \, \text{Sin}[\phi] - \text{Cos}[2\,\beta] \, \text{Cos}[\theta] \, \text{Sin}[\phi]) \, \chi_{yyz};$$

$$\text{c1yop}[\theta\_, \phi\_, \beta\_] := -\text{Sin}[\theta] \, \text{Cos}[\phi] \, \gamma_{yx};$$

$$\text{l1yop}[\theta\_, \phi\_, \beta\_] := \frac{1}{2} \text{Sin}[\theta] \, (\text{Cos}[2\,\beta] \, \text{Cos}[\phi] + \text{Sin}[2\,\beta] \, \text{Cos}[\theta] \, \text{Sin}[\phi]) \, \chi_{yyz};$$

$$\text{l2yop}[\theta\_, \phi\_, \beta\_] := \frac{1}{2} \text{Sin}[\theta] \, (\text{Sin}[2\,\beta] \, \text{Cos}[\phi] - \text{Cos}[2\,\beta] \, \text{Cos}[\theta] \, \text{Sin}[\phi]) \, \chi_{yyz};$$

```
(* in-plane symmetry breaking (along y-direction) *)
(* for jx *)
dxip[θ_, ϕ_, β_] := 1 / 4 (-2 Sin[θ]^2 Sin[2 ϕ] -
      2 Cos[θ] Cos[2 ϕ] Sin[2 β] + 1/2 Cos[2 β] (3 + Cos[2 θ]) Sin[2 ϕ]) χxxy;
c1xip[θ_, ϕ_, β_] := -Cos[θ] γxz;
l1xip[θ_, ϕ_, β_] :=
  1 / 4 (-2 Cos[2 β] Cos[θ] Cos[2 ϕ] - 1/2 (3 + Cos[2 θ]) Sin[2 β] Sin[2 ϕ]) χxxy;
l2xip[θ_, ϕ_, β_] :=
  1 / 4 (-2 Cos[θ] Cos[2 ϕ] Sin[2 β] + 1/2 Cos[2 β] (3 + Cos[2 θ]) Sin[2 ϕ]) χxxy;
(* for jy *)
dyip[θ_, ϕ_, β_] :=
  χyxx 1/4 (Cos[β]^2 (3 Cos[θ]^2 Cos[ϕ]^2 + Sin[ϕ]^2) + Sin[β]^2 (Cos[θ]^2 Cos[ϕ]^2 + 3 Sin[ϕ]^2) +
      Cos[θ] Sin[2 β] Sin[2 ϕ]) + χyyy (1/4 (Sin[β]^2 (3 Cos[ϕ]^2 + Cos[θ]^2 Sin[ϕ]^2) +
        Cos[β]^2 (Cos[ϕ]^2 + 3 Cos[θ]^2 Sin[ϕ]^2) - Cos[θ] Sin[2 β] Sin[2 ϕ]));
c1yip[θ_, ϕ_, β_] := 0;
l1yip[θ_, ϕ_, β_] :=
  χyxx (1/4 (-Cos[θ]^2 Cos[ϕ]^2 Sin[2 β] + Sin[2 β] Sin[ϕ]^2 + Cos[2 β] Cos[θ] Sin[2 ϕ])) +
   χyyy (1/4 (Sin[2 β] (Cos[ϕ]^2 - Cos[θ]^2 Sin[ϕ]^2) - Cos[2 β] Cos[θ] Sin[2 ϕ]));
l2yip[θ_, ϕ_, β_] :=
  χyxx (1/4 (Cos[2 β] (Cos[θ]^2 Cos[ϕ]^2 - Sin[ϕ]^2) + Cos[θ] Sin[2 β] Sin[2 ϕ])) +
   χyyy (1/4 (Cos[2 β] (-Cos[ϕ]^2 + Cos[θ]^2 Sin[ϕ]^2) - Cos[θ] Sin[2 β] Sin[2 ϕ]));
```

ψ is defined as the angle between the x - direction and the direction of current flow collected by the contacts, as shown in Fig. 1C.

```
(* here are the total (d,c1,l1,l2) coefficients *)
d[θ_, ϕ_, β_, ψ_] :=
  (dxop[θ, ϕ, β] + dxip[θ, ϕ, β]) Cos[ψ] + (dyop[θ, ϕ, β] + dyip[θ, ϕ, β]) Sin[ψ];
c1[θ_, ϕ_, β_, ψ_] := (c1xop[θ, ϕ, β] + c1xip[θ, ϕ, β]) Cos[ψ] +
   (c1yop[θ, ϕ, β] + c1yip[θ, ϕ, β]) Sin[ψ];
l1[θ_, ϕ_, β_, ψ_] := (l1xop[θ, ϕ, β] + l1xip[θ, ϕ, β]) Cos[ψ] +
   (l1yop[θ, ϕ, β] + l1yip[θ, ϕ, β]) Sin[ψ];
l2[θ_, ϕ_, β_, ψ_] := (l2xop[θ, ϕ, β] + l2xip[θ, ϕ, β]) Cos[ψ] +
  (l2yop[θ, ϕ, β] + l2yip[θ, ϕ, β]) Sin[ψ]

(* get expressions for (d,c1,l1,l2) in the commonest case β=0, ϕ=90° *)
tϕ = Pi / 2;
tβ = 0;

d = 1/4 Sin[ψ] (χyxx + 3 Cos[θ] (Cos[θ] χyyy - 2 Sin[θ] χyyz))
```

$$c1 = \text{Cos}[\psi]\ \left(\text{Sin}[\theta]\ \gamma_{xy} - \text{Cos}[\theta]\ \gamma_{xz}\right)$$

$$l1 = \frac{1}{2}\ \text{Cos}[\psi]\ \left(\text{Cos}[\theta]\ \chi_{xxy} - \text{Sin}[\theta]\ \chi_{xxz}\right)$$

$$l2 = -\frac{1}{4}\ \text{Sin}[\psi]\ \left(\chi_{yxx} - \text{Cos}[\theta]^2\ \chi_{yyy} + \text{Sin}[2\,\theta]\ \chi_{yyz}\right)$$

```
(* get expressions for (D,C1,L1,L2) in the commonest case β=0, ϕ=0 *)
tϕ = 0;
tβ = 0;
```

$$d = \frac{1}{4}\ \left(-6\,\text{Cos}[\theta]\ \text{Cos}[\psi]\ \text{Sin}[\theta]\ \chi_{xxz} + \text{Sin}[\psi]\ \left(3\,\text{Cos}[\theta]^2\ \chi_{yxx} + \chi_{yyy}\right)\right)$$

$$c1 = -\text{Cos}[\theta]\ \text{Cos}[\psi]\ \gamma_{xz} - \text{Sin}[\theta]\ \text{Sin}[\psi]\ \gamma_{yx}$$

$$l1 = \frac{1}{2}\ \left(-\text{Cos}[\theta]\ \text{Cos}[\psi]\ \chi_{xxy} + \text{Sin}[\theta]\ \text{Sin}[\psi]\ \chi_{yyz}\right)$$

$$l2 = \frac{1}{4}\ \left(-2\,\text{Cos}[\theta]\ \text{Cos}[\psi]\ \text{Sin}[\theta]\ \chi_{xxz} + \text{Sin}[\psi]\ \left(\text{Cos}[\theta]^2\ \chi_{yxx} - \chi_{yyy}\right)\right)$$

```
(* let's get two special cases at θ=30°, ϕ=0⁰ and 90° )
(* here are expressions for (d,c1,l1,l2) at θ=30°, ϕ=0⁰ *)
tθ = Pi / 6;
tβ = 0;
tϕ = 0;
```

$$d = \frac{1}{16}\ \left(-6\,\sqrt{3}\ \text{Cos}[\psi]\ \chi_{xxz} + 9\,\text{Sin}[\psi]\ \chi_{yxx} + 4\,\text{Sin}[\psi]\ \chi_{yyy}\right)$$

$$c1 = \frac{1}{2}\ \left(-\sqrt{3}\ \text{Cos}[\psi]\ \gamma_{xz} - \text{Sin}[\psi]\ \gamma_{yx}\right)$$

$$l1 = \frac{1}{4}\ \left(-\sqrt{3}\ \text{Cos}[\psi]\ \chi_{xxy} + \text{Sin}[\psi]\ \chi_{yyz}\right)$$

$$l2 = \frac{1}{16}\ \left(-2\,\sqrt{3}\ \text{Cos}[\psi]\ \chi_{xxz} + 3\,\text{Sin}[\psi]\ \chi_{yxx} - 4\,\text{Sin}[\psi]\ \chi_{yyy}\right)$$

```
(* here are expressions for (d,c1,l1,l2) at θ=30°, ϕ=90° *)
tθ = Pi / 6;
tβ = 0;
tϕ = Pi / 2;
```

$$d2 = \frac{1}{16}\ \text{Sin}[\psi]\ \left(4\,\chi_{yxx} + 9\,\chi_{yyy} - 6\,\sqrt{3}\ \chi_{yyz}\right)$$

$$c1 = \frac{1}{2}\ \text{Cos}[\psi]\ \left(\gamma_{xy} - \sqrt{3}\ \gamma_{xz}\right)$$

$$l1 = \frac{1}{4}\ \text{Cos}[\psi]\ \left(\sqrt{3}\ \chi_{xxy} - \chi_{xxz}\right)$$

$$l2 = -\frac{1}{16}\ \text{Sin}[\psi]\ \left(4\,\chi_{yxx} - 3\,\chi_{yyy} + 2\,\sqrt{3}\ \chi_{yyz}\right)$$